Combining of Mie-Raman and fluorescence observations: a step forward in aerosol classification with lidar technology

Igor Veselovskii[1], Qiaoyun Hu[2], Philippe Goloub[2], Thierry Podvin[2], Boris Barchunov[1], Mikhail Korenskii[1]

[1]*Prokhorov General Physics Institute of the Russian Academy of Sciences, Moscow, Russia.*

[2]*Univ. Lille, CNRS, UMR 8518 - LOA - Laboratoire d'Optique Atmosphérique, F-59650 Lille, France*

Correspondence: Qiaoyun Hu (qiaoyun.hu@univ-lille.fr)

Abstract

The paper presents an approach to reveal variability of aerosol type at high spatio-temporal resolution, by combining fluorescence and Mie-Raman lidar observations. The multi-wavelength Mie-Raman lidar system in operation at the ATOLL platform, Laboratoire d'Optique Atmosphérique, University of Lille, includes, since 2019, a wideband fluorescence channel allowing the derivation of the fluorescence backscattering coefficient β_F. The fluorescence capacity G_F, which is the ratio of β_F to the aerosol backscattering coefficient, is an intensive particle property, strongly changing with aerosol type, thus providing a relevant basis for aerosol classification. In this first stage of research, only two intensive properties are used for classification: the particle depolarization ratio at 532 nm, δ_{532}, and the fluorescence capacity, G_F. These properties are considered because they can be derived at high spatio-temporal resolution and are quite specific to each aerosol type. In particular, in this study, we use δ_{532} - G_F diagram to identify smoke, dust, pollen and urban aerosol particles. We applied our new classification approach to lidar data obtained during 2020 – 2021 period, which includes strong smoke, dust and pollen episodes. The particle classification was performed with height resolution about 60 m and temporal resolution better than 8 minutes.

1. Introduction

Atmospheric aerosol is one of the key factors influencing the Earth's radiation budget through absorption and scattering of solar radiation and by affecting cloud formation. The processes of aerosol–radiation and aerosol-cloud interaction depend on aerosol size, shape, morphology,

absorption, solubility, etc., thus knowledge of the chemical composition and mixing state of the aerosol particles is important for modeling of aerosol impact (Boucher et al., 2013). The aerosol properties may vary in a wide range, so in practice usually several main types of aerosols are separated on a base of their origin: e.g. urban, dust, marine, biomass burning (Dubovik et al., 2002). Successful remote characterization of column integrated aerosol composition from the observations of Sun – sky photometers and space-borne multiangle polarimeters was demonstrated in numerous publications (Dubovik et al., 2002; Giles et al., 2012; Hamill et al., 2016; Schuster et al., 2016; Li et al., 2019; Zhang et al., 2020). The aerosol impacts, however, depends also on vertical variations/distributions of particle concentration and composition, which cannot be derived from these instruments.

One of the recognized remote sensing techniques for vertical profiling of aerosol properties is a lidar. Multiwavelength Mie-Raman and HSRL (High Spectral Resolution Lidar) lidar systems provide unique opportunity to derive height-resolved particle intensive properties, such as lidar ratios, Angstrom exponents and depolarization ratios at multiple wavelengths. Based on this information, particle type can be determined (Burton et al., 2012, 2013; Groß et al., 2013; Mamouri et al., 2017; Papagiannopoulos et al., 2018; Nicolae et al., 2018; Hara et al., 2018; Voudouri et al., 2019; Wang et al., 2021; Mylonaki et al., 2021 and references therein). However, there is a fundamental difference between particle classification based on the Sun – sky photometer and on lidar observations. From both direct Sun and azimuth scanning measurements of the photometer more than 100 observations are available. From this information the spectrally dependent refractive index and absorption Angstrom exponent can be determined, which is important for aerosol classification (Schuster et al., 2016; Li et al., 2019). The commonly used multiwavelength lidars are based on a tripled Nd:YAG laser and are capable of providing three backscattering (355 nm, 532 nm, 1064 nm), two extinction (355 nm, 532 nm) coefficients and up to three particle depolarization ratios (so called $3\beta+2\alpha+3\delta$ set). Thus the number of available lidar observations is eight or less, which limits the performance of the aerosol typing algorithms. Nevertheless, the results obtained by different research groups demonstrate that lidar-based particle identification is possible. In publications of Burton et al. (2012, 2013) classification was performed from four intensive parameters measured by the HSRL system: the lidar ratio at 532 nm (S_{532}), the backscattering Angstrom exponent for 532/1064 nm wavelengths ($BAE_{532/1064}$), and particle depolarization ratios at 532 nm and 1064 nm (δ_{532}, and δ_{1064}). With these input parameters eight

aerosol types: smoke, fresh smoke, urban, polluted maritime, maritime, dusty mix, pure dust and ice were discriminated.

Important information on aerosol vertical distribution comes from the EARLINET/ACTRIS lidar-network, aiming at unifying multiwavelength Mie-Raman lidar systems over Europe (Pappalardo et al., 2014). For the automation of aerosol classification, several approaches were developed in the frame of EARLINET. These approaches include the Mahalanobis distance-based typing algorithm (Papagiannopoulos et al., 2018), a neural network aerosol classification algorithm (NATALI) (Nicolae et al., 2018), and algorithm based on source classification analysis (SCAN) (Mylonaki et al., 2021). All these algorithms have demonstrated their ability for aerosol classification. In particular, the NATALI is able to identify up to 14 aerosol mixtures from 3β+2α+1δ observations.

Nevertheless, the above-mentioned algorithms have to deal with a fundamental limitation: the particle intensive properties, even for pure aerosols (generated by a single source) exhibit strong variations. For example, the lidar ratio S_{355} of smoke in publication of Nicolae et al. (2018) varies in 38 sr – 70 sr range, and in our own measurements we observed for aged smoke S_{355} as low as 25 sr (Hu et al., 2021). Strong variation of smoke lidar ratios in EARLINET/ACTRIS observations is discussed also in the recent publication of Adam et al. (2021). Such uncertainty in parameters of the aerosol model complicates the aerosol classification. Thus, it is desirable to combine the Mie-Raman observations with another range resolved technique, providing additional independent information about aerosol composition. Such information can be obtained from laser induced fluorescence emission.

Application of fluorescence lidar technique was intensively considered during the last decade to study aerosol particles. Lidar measurements of the full fluorescence spectrum with multianode photomultipliers (Sugimoto et al., 2012; Reichardt et al., 2014, 2017; Saito et al., 2022) provides an obvious advantage in particle identification. However, even a more simple fluorescence lidar with a single wideband fluorescence channel, opens new opportunities for aerosol characterization (Veselovskii et al., 2021; 2022; Zhang et al., 2021). Such fluorescence configuration could be implemented in existing Mie-Raman lidars, and the fluorescence backscattering coefficient β_F is calculated from the ratio of fluorescence and nitrogen Raman signals. To characterize the aerosol fluorescence properties, the fluorescence capacity G_F is introduced as the ratio of β_F to aerosol backscattering coefficient at one of laser wavelengths

(Veselovskii et al., 2020b). In this study, the backscattering at 532 nm was used. The fluorescence capacity is an intensive particle parameter, which changes strongly with aerosol type, being the highest for smoke and the lowest for dust. Thus, the combination of Mie – Raman and fluorescence backscatter provides a basis to improve particle classification. A Mie – Raman lidar provides several particle intensive parameters, however, the profiles of particle parameters associated with the extinction coefficient, such as lidar ratio or extinction Angstrom exponent, may contain strong noises, because the extinction coefficients are derived from the slope of Raman lidar signals, thus averaging over significant spatio-temporal intervals is demanded. Meanwhile, the particle depolarization and the fluorescence *capacity* can be calculated with high spatio-temporal resolution.

Recently, we have demonstrated that the $\delta - G_F$ diagram allows to separate several aerosol types, such as dust, pollen, urban (continental) and smoke (Veselovskii et al., 2021a). In the present study, we use this technique to classify aerosol particle types in the troposphere at high spatio-temporal resolution. We present results of aerosol classification on the basis of fluorescence and Mie-Raman lidar measurements performed at the ATOLL (ATmospheric Observation at liLLe) at Laboratoire d'Optique Atmosphérique, University of Lille, during 2020 – 2021 period, which includes strong smoke, dust and pollen episodes. Paper starts with a description of the experimental setup and data processing scheme in Sect.2. In Sect.3 we present the algorithm for aerosol classification on a base of depolarization and fluorescence measurements. Results of the application of the developed approach to different atmospheric situations, including smoke, dust and pollen episodes are given in Sect.4.

2. Experimental setup and data analysis

2.1. Lidar system

The multiwavelength Mie-Raman lidar LILAS (LIlle Lidar AtmosphereS) is based on a tripled Nd:YAG laser with a 20 Hz repetition rate and pulse energy of 70 mJ at 355 nm. Backscattered light is collected by a 40 cm aperture Newtonian telescope and the lidar signals are digitized with Licel transient recorders with 7.5 m range resolution, allowing simultaneous detection in the analog and photon counting mode. The system is designed for the detection of elastic and Raman backscattering, allowing the so called $3\beta+2\alpha+3\delta$ data configuration, including three particle backscattering (β_{355}, β_{532}, β_{1064}), two extinction (α_{355}, α_{532}) coefficients along with

three particle depolarization ratios (δ_{355}, δ_{532}, δ_{1064}). The particle depolarization ratio, determined as a ratio of cross- and co-polarized components of the particle backscattering coefficient, was calculated and calibrated in the same way as described in Freudenthaler et al. (2009). Many calibration and operation procedures have been automated for the LILAS system to improve the overall performance of the lidar in terms of observation frequency and data quality. The aerosol extinction and backscattering coefficients at 355 and 532 nm were calculated from Mie-Raman observations (Ansmann et al., 1992), while β_{1064} was derived by the Klett method (Klett, 1985). The full geometrical overlap was achieved at approximately 750 m range. For calculation of α and β at 532 nm we use the rotational Raman scattering instead of the vibrational one (Veselovskii et al., 2015), which allows to increase the power of Raman backscatter and to decrease separation between the wavelengths of elastic and Raman components. Additional information about atmospheric parameters was available from radiosonde measurements performed at Herstmonceux (UK) and Beauvechain (Belgium) stations, located 160 km and 80 km away from the observation site respectively.

The LILAS system can also profile the laser induced fluorescence of aerosol particles. A part of the fluorescence spectrum is selected by a wideband interference filter of 44 nm width centered at 466 nm. The strong sunlight background at daytime restricts the fluorescence observations to nighttime hours. The fluorescence backscattering coefficient $\beta_{F,}$ is calculated from the ratio of fluorescence and nitrogen Raman backscattering signal, as described in Veselovskii et al. (2020b). This approach allows us to evaluate the absolute values of $\beta_{F,}$ if the relative sensitivity of the channels is calibrated and the nitrogen Raman scattering differential cross section is known. All β_F profiles presented in this work were smoothed with the Savitzky – Golay method, using second order polynomials with 21 points in the window. For the calculation of the fluorescence capacity G_F, in principle, backscattering coefficients at any laser wavelength can be used. In our study we always used β_{532}, because it is calculated with the use of rotational Raman component and is considered to be the most reliable, thus the fluorescence capacity is calculated as $G_F = \frac{\beta_F}{\beta_{532}}$.

2.2.Calculation of the particle backscattering coefficient from Mie-Raman measurements

Mie – Raman lidar measurements allow independent evaluation of aerosol extinction and backscattering coefficients. Commonly used approach for β calculation was formulated in the paper of Ansmann et al. (1992). This approach includes the choice of a reference height, where the

scattering is purely molecular. However, such height range is not always available, for example, in the presence of the low level clouds. Moreover, when long-term spatio-temporal variations of backscattering coefficients are analyzed, the uncertainty in the choice of the reference height leads to oscillations in β profiles. To resolve this issue, we modified the Raman method as described below.

In an elastic channel, the backscattered radiative power P_L, at wavelength λ_0 and distance z is described by the lidar equation:

$$P_L = O(z)\frac{1}{z^2}C_L(\beta_L^a + \beta_L^m)\exp\left\{-2\int_0^z(\alpha_L^a + \alpha_L^m)dz'\right\} = O(z)\frac{1}{z^2}C_L(\beta_L^a + \beta_L^m)T_L^2, \quad (1)$$

while in a Raman channel, it can be written as:

$$P_R = O(z)\frac{1}{z^2}C_R\beta_R\exp\left\{-\int_0^z(\alpha_L^a + \alpha_R^a + \alpha_L^m + \alpha_R^m)dz'\right\} = O(z)\frac{1}{z^2}C_R\beta_R T_L T_R. \quad (2)$$

Here O(z) is the geometrical overlap factor, which is assumed to be the same for elastic and Raman channels. C_L and C_R are the range independent constants, including efficiency of the detection channel. T_L and T_R are one-way transmissions, describing light losses on the way from the lidar to distance z at laser λ_L and Raman λ_R wavelengths. Backscattering and extinction coefficients contain aerosol and molecular contributions: $\beta_L^a + \beta_L^m$ and $\alpha_L^a + \alpha_L^m$, where the superscripts "a" and "m" indicate aerosol and molecular scattering, respectively. Raman backscattering coefficient is:

$$\beta_R = N\sigma_R, \quad (3)$$

where N is the number of Raman scatters (per unit of volume) and σ_R is the Raman differential scattering cross section in the backward direction.

Dividing equation (1) on (2) we get:

$$\frac{P_L}{P_R} = \frac{C_L}{C_R}\frac{(\beta_L^a + \beta_L^m)}{\beta_R}\frac{T_L}{T_R} \quad (4)$$

Backscattering coefficient is calculated from (3) and (4) as:

$$\beta_L^a = \frac{P_L}{P_R}\frac{C_R}{C_L}\sigma_R N\frac{T_R}{T_L} - \beta_L^m = \frac{P_L}{P_R}KN\frac{T_R}{T_L} - \beta_L^m \quad (5)$$

178 The differential transmission $\frac{T_L}{T_R}$ can be calculated the same way, as it is done for the water vapor
179 measurements (Whiteman, 2003). For rotational Raman signal, which we use in our 532 nm
180 channel (Veselovskii et al., 2015), $\lambda_L \approx \lambda_R$, so $\frac{T_L}{T_R}=1$.

181 The calibration constant $K = \frac{C_R}{C_L}\sigma_R$ can be found by comparing β_L^a in Eq.5 with the
182 backscattering coefficient $\tilde{\beta}_L^a$ computed with the traditional Raman method, using the reference
183 height (Ansmann et al., 1992).

184 $$K = (\tilde{\beta}_L^a + \beta_L^m)\frac{P_R}{P_L}\frac{1}{N}\frac{T_L}{T_R} \quad (6)$$

185 For simplicity, hereinafter we will use notation β_L instead β_L^a. Thus, if during the measurement
186 session we have a temporal interval, where the reference height is available, we can determine the
187 calibration constant *K* and use it for β_L calculations from eq.5, assuming that relative sensitivity of
188 channels during the session is not changed. Even if cloud layers occur during the whole session,
189 we can use *K* from the previous cloud-free profiles (assuming, again, that the relative sensitivity
190 of channels is the same). We will call this approach for β calculation as "modified Raman method",
191 to distinguish it from traditional one (Ansmann et al., 1992).

192 To estimate variations of the relative sensitivity of the channels, we analyzed long-term
193 cloudless measurements when the reference height was available for every individual profile. The
194 results demonstrate that variations of calibration constant during the session (about 8 hours) were
195 below 3%. Fig.1 and 2 present the application of this modified Raman method to the measurements
196 on 2 March 2021. The dust layer extended from 2 km to 8 km height and inside this layer the ice
197 and liquid clouds were formed during the 00:00 – 05:00 UTC interval, thus β_{532} could not be
198 calculated with traditional Raman technique. The temporal interval 19:00 – 20:00 was used to find
199 calibration constant *K*. Fig.1 shows vertical profiles of backscattering coefficient $\tilde{\beta}_{532}$ calculated
200 with traditional Raman method (with reference height), and β_{532} calculated with modified method
201 (with the calibration constant). Profiles of $\tilde{\beta}_{532}$ and β_{532} coincide for the whole height range. The
202 calibration constant *K*, shown on the same plot, does not demonstrate height dependence, though

oscillations around the mean value increase with height. For computations, we choose the value of K at low altitudes averaged inside some height interval.

Fig.2 provides spatio-temporal variations of β_{532}, particle depolarization δ_{532} and the fluorescence capacity G_F. Depolarization measurements reveal the presence of dust ($\delta_{532}\approx30\%$) and the ice cloud above 4 km ($\delta_{532}>40\%$). The liquid cloud below 4 km after midnight can be identified by a low depolarization ratio $\delta_{532}<3\%$. The fluorescence capacity of dust is low, about 0.2×10^{-4}. However, below 2 km, G_F is significantly higher, up to 1.2×10^{-4}. In combination with a high depolarization ratio (up to 20%), it can indicate the presence of pollen at low altitudes. On the fluorescence capacity panel, we can see that after 01:00 UTC the dust and pollen layers are mixed below 2 km, resulting in a value of G_F about 0.5×10^{-4}. The fluorescence capacity inside ice and liquid clouds is below 0.01×10^{-4}. Fig.2 clearly demonstrates the advantage of simultaneous depolarization and fluorescence measurements for the study of cloud formation in the presence of aerosol. All spatio-temporal distributions of β_{532} presented in this paper were calculated from Eq.5 with a modified Raman method.

3. Aerosol classification based on fluorescence measurements

3.1. *Approach for aerosol classification*.

As was discussed in our recent publication (Veselovskii et al., 2021), the δ-G_F diagram allows to separate several aerosol types, including smoke, dust, pollen, urban, ice and liquid water particles. Smoke and urban aerosols both have a small depolarization ratio, but the fluorescence capacity of smoke is almost one order higher, so these particles can be separated. Dust and pollen both have high depolarization ratio (up to 30%), but G_F of dust is significantly lower, which again provides basis for discrimination. The depolarization ratio of some aerosol types is characterized by strong spectral dependence. For example, the depolarization ratio of aged smoke decreases with wavelength. It is below 5% at 1064 nm but at 355 nm in upper troposphere it may exceed 20% (Burton et al., 2015; Haarig et al., 2018; Hu et al., 2019; Veselovskii et al., 2022), which complicates smoke and dust separation. For pollen, on the contrary, the depolarization ratio at 1064 nm can be the highest (Veselovskii et al., 2021). Thus, choice of δ_{1064} for δ-G_F diagram could be advantageous. However, as mentioned, the backscattering coefficient at 1064 nm is calculated with Klett method (Klett, 1985), which, besides assumption about lidar ratio, needs reference

height and cannot be used in cloudy situations. This is why in our study we used the δ_{532}-G_F diagram.

In our present work, we consider a simple classification scheme since we use only two intensive parameters G_F and δ_{532}. Our goal is to demonstrate that in the δ_{532}-G_F diagram, our lidar observations form clusters and characteristic patterns which can be attributed to different aerosol types or their mixtures. We consider four aerosol types: dust, smoke, pollen and urban, and two cloud types: liquid and ice clouds. Dust and pollen are large particles of complicated shape, characterized by high depolarization ratio, while smoke and urban pollution are small particles with low depolarization. In our classification "urban aerosol" includes continental aerosol, sulfates and soot. At this stage, we do not yet consider absorption to discriminate particles.

The choice of the range of particle properties variation for each aerosol type is an important aspect of the approach. Typical ranges of G_F and δ_{532} variations used in our classification scheme are given in Table 1 and are shown in Fig.3. These ranges are based on results obtained in LOA (Laboratoire d'Optique Atmosphérique) and on results presented in aerosol classification studies (Burton et al., 2012, 2013; Nicolae et al., 2018; Papagiannopoulos et al., 2018, Mylonaki et al., 2021).

Dust. The depolarization ratio, δ_{532}, of Saharan dust near the source regions is up to 35% (Veselovskii et al., 2020a). However, after transportation and mixing with local aerosol δ_{532} can be as low as 20% (Rittmeister et al., 2017). In many studies, the dust events having with smaller depolarization ratio are classified as "polluted dust" (e.g. Burton et al., 2012, 2013). At the moment, we do not introduce the discrimination between the two subtypes and mark as "dust" the particles with $20\%<\delta_{532}<35\%$, and $0.1\times10^{-4}<G_F<0.5\times10^{-4}$.

Smoke. In 2021-2022, we regularly observed, over ATOLL platform, smoke layers originated from Californian and Canadian forest fires (Hu et al., 2022). The particle depolarization and fluorescence capacity of this transported smoke varied from episode to episode and, for classification, we selected the ranges $2\%<\delta_{532}<10\%$, $2\times10^{-4}<G_F<6\times10^{-4}$. At this stage, we do not discriminate "fresh" and "aged" smoke, and the range of δ_{532} variation is similar to the one used in classification of Burton et al. (2012).

Pollen. The pollen over north of France is usually mixed with other aerosol and the particles which we mark as "pollen" are actually the mixtures. Depolarization ratio of clean pollen varies strongly for different taxa. For birch pollen, Cao et al. (2010) reported δ_{532}=33%, and in the

measurements over Finland during birch pollination (Bohlmann et al., 2019), observed values of δ_{532} up to 26%. The observations over Lille during pollen season (Veselovskii et al., 2021a) rarely revealed values δ_{532} exceeding 20%. Based on that observations, we type as "pollen" the particles mixtures with $15\%<\delta_{532}<30\%$, and $0.8\times10^{-4}<G_F<3.0\times10^{-4}$.

Urban. This type of aerosol includes a variety of particle types (e.g. sulfates, soot) and its properties may depend on the relative humidity. Based on our measurements inside the boundary layer, for classification we choose the ranges $1\%<\delta_{532}<10\%$, and $0.1\times10^{-4}<G_F<1.0\times10^{-4}$. Similar range for δ_{532} is used in classification of Burton et al. (2013). Urban and smoke particles both have a low depolarization, but the smoke fluorescence capacity can be up to one order higher, so these particles can be reliably discriminated.

Ice and water clouds. Both cloud types have low fluorescence capacity $G_F<0.01\times10^{-4}$. However, the ice clouds are usually observed at the heights, where fluorescence signal is low and can not be used for classification. Thus above ~8 km, the ice cloud are identified by high depolarization ratio $\delta_{532}>40\%$. Depolarization ratio of the liquid water clouds is usually affected by the effects of the multiple scattering, so for their identification we use $\delta_{532}<5\%$.

The analysis of aerosol mixtures is an important subject and, the possibility to separate the mixture components based on lidar measurements was discussed in publications of Sugimoto and Lee (2006), Gross et al. (2011), Gasteiger et al. (2011), Tesche et al. (2009), Burton et al. (2014). The information about mixture composition can be also revealed in δ_{532}-G_F diagram. For example, pollen can be mixed with urban particles. At different heights the pollen contributes differently to β_{532}, so at δ_{532}-G_F diagram, the data points will form the pattern, which extends from location, attributed to "pure" urban aerosol to location, attributed to "pure" pollen. To estimate, how such pattern looks like, a simplified modeling for fixed particle parameters was performed. Corresponding results are shown in Fig.3 by symbols (circles). The particle depolarization ratio δ of the mixture, containing urban aerosol (u) and pollen (p), with depolarization ratios δ^u and δ^p, can be calculated as:

$$\delta = \frac{\left(\frac{\delta^p}{1+\delta^p}\right)\beta^p + \left(\frac{\delta^u}{1+\delta^u}\right)\beta^u}{\frac{\beta^p}{1+\delta^p} + \frac{\beta^u}{1+\delta^u}} \quad (7)$$

The fluorescence capacity of the mixture is given by:

$$G_F = \frac{\beta^u G_F^u + \beta^p G_F^p}{\beta} \quad (8)$$

Here total backscattering $\beta = \beta^u + \beta^p$.

The computations in Fig.3 were performed for values of pollen contribution $\frac{\beta_{532}^p}{\beta_{532}}$ in 0 - 1.0 range with step 0.1. We assume that the depolarization ratios of pollen and urban aerosol are δ_{532}^p =30% and δ_{532}^u =3%, while the fluorescence capacities are G_F^u =0.2×10^{-4} and G_F^p =2.5×10^{-4}. We remind that the fluorescence capacities are calculated at 532 nm wavelength. In the δ_{532}-G_F diagram the computed points provide a characteristic curve, which in the next section will be compared with experimental results. The same computations were performed for a smoke (s) and dust (d) mixture, assuming δ_{532}^d =30%, δ_{532}^s =3%, G_F^d =0.2×10^{-4} and G_F^s =4.0×10^{-4}. Corresponding results are shown in Fig.3 with stars. In a similar way, the characteristic curves for other mixtures can be also represented.

We are also able to identify liquid water and ice layers. Liquid water cloud layers have low fluorescence capacity (G_F<0.01×10^{-4}) and δ_{532}<3%. Ice particles also have low G_F, but at heights where ice clouds are usually observed, the signal of fluorescence backscattering is noisy. Thus at high altitudes ice particles are discriminated by a high depolarization ratio δ_{532}>40 %.

3.2. *Classification of spatio-temporal observations*

The input parameters in our classification scheme are the spatio-temporal distributions of β_{532}, δ_{532} and G_F, which are presented as matrices $\beta_{532}^{i,j}$, $\delta_{532}^{i,j}$, $G_F^{i,j}$, where i=1… N_T; j=1… N_H. Values N_T and N_H are the numbers of temporal and height intervals in the analyzed dataset. In a single measurement we accumulate 2×10^3 laser pulses, so temporal resolution of the measurements is about 100 s, while the height resolution is 7.5 m.

The particle intensive properties cannot be evaluated reliably when the backscattering coefficient is low. Thus, we set a threshold value for β_{532} (normally 0.2 Mm^{-1}sr^{-1}); namely, when $\beta_{532}^{i,j}$ < 0.2 Mm^{-1}sr^{-1} the elements of the matrices $\delta_{532}^{i,j}$ and $G_F^{i,j}$, are classified as "low signal" and ignored. For the remaining elements, we determine the aerosol type, using our approach. A primary typing is being made for each point *(i,j)* separately, in accordance with parameter ranges given in

the Table 1. The elements, which are out of all these ranges, are marked as “undefined”. We consider 6 types of the particles, respectively dust, smoke, pollen, urban, ice crystals and water droplets. Moreover, there can be two additional results of primary typing: “undefined” and “low signal”. Thus, there are altogether 8 possible results of primary typing. For every aerosol type, a $N_T \times N_H$ dimension matrix is constructed. If at this first stage of classification some single pixel point (i, j) is classified as, e.g., dust, the corresponding value in the 'dust' matrix is set to 1, otherwise it is set to 0.

The single pixel particle parameters contain statistical noise, which influences the results of the primary typing, thus producing high frequency oscillations of non-physical character. From a physical point of view, the aerosol single-type areas should form smooth regions, so a special smoothing procedure (stage 2 of our algorithm) was developed to remove the oscillations. The smoothing procedure is based on a convolution with Gaussian kernel

$$Z = \exp\left(-\left(\frac{t^2}{s_T^2} + \frac{h^2}{s_H^2}\right)\right) \quad (9)$$

where t and h are temporal and height coordinates. The resolution of typing is being controlled by the parameters s_T and s_H, which are set as the number of temporal and height bins.

On the second stage of classification each of these matrices is separately convoluted with the Gauss kernel Z. After the convolution, the values for each pixel (i,j) are being compared. If, e.g., the 'dust' matrix contains maximal value at the pixel (i,j), in respect to all other matrices, then the pixel (i,j) is finally classified as dust. The choice of smoothing parameters depends on aerosol loading and aerosol type. For the measurements inside the boundary layer in many cases the single pixel typing (s_T=1, s_H=1) is possible, while for analysis of the weak elevated layers the smoothing should be applied. All results presented in this study were obtained for s_T=3 and s_H=5, thus the temporal and range resolutions of our typing procedure are estimated to be about 8 minutes and 60 m respectively.

4. Application of classification approach to LILAS data

The classification approach, described in the previous section, was applied to the data of the Mie-Raman- Fluorescence lidar at the ATOLL platform, located on the campus of Lille University, during 2020 – 2021 period. Here we present results of aerosol classification for several

relevant atmospheric situations, to demonstrate that different aerosol types are well separated based on δ_{532}-G_F diagram.

12 September 2020: Wildfire smoke

Fig.4 presents the spatio-temporal variations of aerosol and fluorescence backscattering coefficients (β_{532} and β_F) together with the particle depolarization ratio δ_{532} and the fluorescence capacity G_F during smoke episode on the night 12-13 September 2020. The smoke layer extends from approximately 2 km to 5 km height, and it is characterized by high fluorescence capacity $G_F > 3.0\times10^{-4}$ and low depolarization ratio $\delta_{532} < 7\%$. The cirrus clouds occurred above 11 km height during the whole night. The smoke layer was transported from North America; detailed analysis of the layer origin and transportation is given in the recent publication of Hu et al. (2022). The results of aerosol typing for this episode are shown in Fig.5. On the δ_{532}-G_F diagram these data form two clusters. First cluster includes points in the range $2.0\times10^{-4} < G_F < 6.0\times10^{-4}$ and $2\% < \delta_{532} < 7\%$, such high fluorescence and low depolarization should be attributed to smoke particles. The second cluster consists of points localized inside $0.1\times10^{-4} < G_F < 0.8\times10^{-4}$ and $1\% < \delta_{532} < 3\%$ intervals which corresponds to urban particles in Table 1. After cluster localization, the observations can be plotted as aerosol types, using the parameters in Table 1 and the approach, described in section 3.2. The aerosol types in Fig.5b are spatially separated and contain no high frequency oscillations. Urban particles are localized at low heights, below 1 km. We would like to remind that, at the condition of high relative humidity (RH), the fluorescence capacity can decrease due to the particle's hygroscopic growth. The water uptake increases the particle backscattering, but does not change the fluorescence. As a result, the fluorescence capacity decreases. (Veselovskii et al., 2020). In accordance with radiosonde data the relative humidity below 1 km was quite high (about 70% at 500 m) and decreased with height, which can explain the wide range of G_F variation observed for urban particles in Fig.5a.

The particle intensive properties, such as the lidar ratios at 355 nm and 532 nm wavelengths (S_{355}, S_{532}), the particle depolarization ratios (δ_{355}, δ_{532}, δ_{1064}), the extinction ($A^{\alpha}_{355/532}$) and the backscattering ($A^{\beta}_{355/532}$, $A^{\beta}_{532/1064}$) Angstrom exponents for the episodes analyzed in this study, are summarized in Table 2. For this measurement session, in the smoke layer the lidar ratio at 532 nm significantly exceeds corresponding value at 355 nm ($S_{532}=80\pm12$ sr and $S_{355}=50\pm7$ sr). The particle depolarization ratio decreases with wavelength from 4.5% at 355 nm to 2% at 1064 nm.

Such spectral dependence of the lidar ratio and depolarization ratio for the aged smoke is in agreement with previous studies (e.g. Haarig et al., 2018; Hu et al., 2022 and references therein).

30 May 2020: Urban vs Pollen

Pollen grains represent a significant fraction of primary biological materials in the troposphere and fluorescence induced emission provides an opportunity for their identification. Fig.6 presents spatio-temporal variations of β_{532}, β_F, δ_{532}, G_F during pollen season on the night 30-31 May 2020. Presence of different types of pollen over Lille in Spring – Summer 2020 was discussed in our recent publication (Veselovskii et al., 2021). In particular, on 30 May 2020 the in situ measurements at the roof of the building demonstrate the presence of significant amount of grass pollen. The transport of pollen can be analyzed with a global-to-meso-scale dispersion model SILAM (Sofiev et al., 2015). In Appendix we show the maps of the pollen index, for four sessions from this study at 22 UTC. On 30 May the pollen index in Lille region is about 5.0, indicating high content of pollen.

The aerosol is located inside the planetary boundary layer (PBL) below 2.5 km. At altitudes below 1 km, the depolarization ratio δ_{532} after 23:00 increases up to ~15% simultaneously with an increase of the fluorescence capacity up to 2.0×10^{-4}, which can be an indication of pollen presence. On the δ_{532}-G_F diagram in Fig.7a, the single pixel data points spread from the values typical for the urban particles to the values typical for the pollen. Contribution of pollen to the total backscattering changes with height and the points form the pattern, similar to characteristic curve, calculated for urban – pollen mixture in Fig.3. In accordance with radiosonde data from Herstmonceux station, the RH at midnight was about 40% at 500 m and it increased up to 70% at 2000 m, thus the spatio – temporal variations of RH could influence the observed values of the backscattering coefficient and depolarization ratio. In particular, the hygroscopic growth can decrease the values of both δ_{532} and G_F. However, the value of the fluorescence capacity in Fig.7a changes for almost one order of magnitude, and such strong change in G_F can not be explained by the particle hygroscopic growth only. For example, from the recent publication of Sicard et al. (2022), increase of β_{532} of urban aerosol for this range of RH, is below the factor 1.5. Thus, we suppose that the pattern in Fig.7a is due to the mixing urban and pollen particles The spatio–temporal distribution of aerosol types is shown in Fig.7b. The urban particles (brown) are

predominant, while pollen (yellow) is localized below 1 km height. The grey color corresponds to unidentified aerosol type which, in our case, is the mixture of urban particles and pollen.

An indicator of pollen presence in an aerosol mixture, along with high depolarization ratio, can be a higher value of δ_{1064} in respect to δ_{532} or δ_{355} (Cao et al., 2010; Veselovskii et al., 2021). Vertical profiles of the particle depolarization ratio at all three wavelengths for this episode are given in Fig.8c of Veselovskii et al. (2021). At 0.75 km height, where δ_{1064} is about 15%, the ratio $\frac{\delta_{1064}}{\delta_{532}}$ is 1.5, which corroborates suggestions about pollen presence. For urban aerosol the depolarization spectral ratio $\frac{\delta_{1064}}{\delta_{532}}$ can be also above 1.0 (Burton et al., 2013), but absolute values of depolarization are significantly lower than for pollen particles (below 10%).

14 September 2020: wildfire smoke vs pollen mixture

Another strong smoke episode occurred in the night 14-15 September 2020, and corresponding distributions of β_{532}, β_F, δ_{532}, and G_F are shown Fig.8. The elevated smoke layer with low depolarization ratio (δ_{532}<5%) and high fluorescence capacity (up to 4.0×10^{-4}) was observed at approximately 6 km height during the whole night. Inside the boundary layer the depolarization ratio is higher, up to 15%, while fluorescence capacity is lower (about 1.0×10^{-4}), compared to the elevated layer. On the δ_{532}-G_F diagram in Fig.9a we can see the cluster of data points, corresponding to the smoke. The same time, a part of the points are inside the range of parameters attributed to the pollen (Table 1). The remaining points should be attributed to the mixture of pollen, smoke and urban aerosol. On the distribution of the particle types (Fig.9b) this mixture is marked with gray color. The pollen particles are localized below 1 km. Presence of pollen over Lille in September is not common, but it can be transported from other regions. The SILAM pollen index in Fig.A1 for this date demonstrates the transport of pollen to northern France from the southeast of France and the east Mediterranean.

Fig.10a presents profiles of δ_{532} and δ_{1064} together with β_{532} for the temporal interval 00:00 – 04:00 UTC. The relative humidity, in accordance with radiosonde data from Herstmonceux station, did not exceed 50% below 1.7 km. Above that height RH increased up to 75% at 2.5 km, thus the observed increase of β_{532} above 1.5 km can be partly related to RH growth. The relative humidity inside the smoke layer did not exceed 10%. Similarly to Fig.8, δ_{1064} exceeds δ_{532} at low

heights. The ratio $\frac{\delta_{1064}}{\delta_{532}}$ is about 1.5 at 1 km and inside the smoke layer $\frac{\delta_{1064}}{\delta_{532}} \approx 0.4$. Higher values of depolarization ratio at 532 nm compared to 1064 nm are reported for aged smoke by Haarig at al. (2018), Hu et al. (2019, 2022). The BAE does not present significant height variations: $A^{\beta}_{532/1064}$ is about 1.0 inside the PBL and it increases to 1.25 inside the smoke layer (Fig.10b). Simultaneously, the fluorescence capacity in the smoke layer increases about a factor 4, comparing to the PBL, which demonstrates efficiency of the fluorescence technique for discriminating smoke from other aerosol types.

10 April 2020: Urban vs Pollen

In the beginning of April, we experienced several atmospheric situations, for which elevated layers were classified as urban aerosols. One of such cases, on the night 10 -11 April 2020, is shown in Fig.11. Lidar observations were performed at an angle of 45 degrees to the horizontal, so the minimum height reachable in the analysis is 350 m. The relative humidity, in accordance with radiosonde data from Herstmonceux station, increased with height from 54% at 1.0 km to 65% at 2.2 km. The layer with depolarization ratio δ_{532} below 5% was observed at about 2 km height during the night. The fluorescence capacity in the layer is low (below 0.5×10^{-4}), so it is identified as urban aerosol. HYSPLIT backward trajectories (not shown) indicate that the air masses at 750 m and 2000 m heights were transported from England (HYSPLIT, 2022). For the period 21:00 – 23:00 UTC the depolarization ratio below 500 m has increased simultaneously with the fluorescence capacity, which can be an indication of pollen presence.

On the δ_{532}-G_F diagram (Fig.12a) the single pixel measurements in 350 m – 1500 m and 1500 m – 2500 m height ranges are shown by different colors. The data points related to the upper layer are within the range of parameters expected for urban aerosol. The points in the lower layer (below 1500 m), are partly out of this range, so the aerosol type for these points is undefined. We assume that this is the mixture of urban and pollen particles, because we observe particles with high depolarization (δ_{532}>15%) and fluorescence capacity up to 0.7×10^{-4}. This mixture is marked by grey color on aerosol mask in Fig.12b. The pollen index provided by SILAM over Lille on the midnight, is above 4.0, so the presence of pollen particles is expectable.

The presence of pollen is supported also by the profiles of δ_{532} and δ_{1064}, shown in Fig.13. At low heights δ_{1064} exceeds δ_{532} and the ratio $\frac{\delta_{1064}}{\delta_{532}}$ is about 1.4 at 0.5 km. However, inside the elevated layer this ratio decreases and becomes about 0.8 at 2.25 km, which indicates that mixture composition changed. For the same height range, the fluorescence capacity decreases from 0.6×10^{-4} to 0.3×10^{-4} while $A^{\beta}_{532/1064}$ gradually increases from 0.75 to 1.25 which can be due to decrease of pollen contribution.

As follows from Table 2, in the lower layer the values of S_{355} and S_{532} are close (about 48±7 sr). However, in elevated layer S_{532} increases to 70±7 sr, while S_{355} remains the same. Higher values of S_{532}, in respect to S_{355}, are typical for aged smoke (e.g. Müller et al., 2005; Hu et al., 2022). Moreover, $A^{\beta}_{355/532}$ significantly exceeds $A^{\alpha}_{355/532}$, which was also reported for aged smoke. Thus, based on intensive properties only, we could classify this layer as "smoke". However, due to low fluorescence capacity, in our approach we identify it as "urban".

11 August 2021: contacting layers of smoke and urban aerosol

Separation of smoke and urban particles is a challenging task for Mie – Raman lidar, because both types have small effective radius, and similar depolarization ratios δ_{532}. However, the fluorescence capacity of smoke is about factor 4-5 higher than that of urban aerosol, which allows their reliable separation. The analyses of the measurements in the night 11-12 August 2021 are shown in Fig.14. The RH decreases with height from 70% to 40% inside 500 m – 2250 m range. The main part of aerosol is concentrated below 2500 m and two height intervals can be distinguished. Above approximately 1500 m the layer with high fluorescence capacity (up to 3.0×10^{-4}) is observed, while in the layer below 1500 m, the G_F is low, (below 0.8×10^{-4}). HYSPLIT backward trajectories (not shown) indicate that the air masses at 1800 m heights were transported from North America, so these may contain wield fire smoke.

On the δ_{532}-G_F diagram (Fig.15a) the single pixel measurements in 500 m – 1400 m and 1400 m – 2500 m height ranges are shown by different colors. The cluster of points, corresponding to the upper layer, is localized mainly inside the interval $1.8\times10^{-4}<G_F<4.0\times10^{-4}$ and $4\%<\delta_{532}<10\%$, and can be attributed to smoke. The points corresponding to the lower layer are partly identified as urban particles, but a part of the points is out of the range and forms a pattern typical for urban – pollen mixture. The SILAM pollen index in Fig.A1 is above 5.0, so contribution of pollen can

be noticeable. The smoke and urban layers are in contact and the particle mixing occurs, which increases dispersion within the clusters.

Vertical profiles of δ_{532} and $A^{\beta}_{532/1064}$ in Fig.16 do not demonstrate significant difference for upper and lower layers. Meanwhile, the fluorescence capacity increases by factor 4. The lidar ratios S_{355} and S_{532} in the upper layer, as follows from Table 2, are 45±7 sr and 72±11 sr respectively. The $A^{\beta}_{355/532}$ significantly exceeds $A^{\alpha}_{355/532}$ (2.2±0.2 and 1.0±0.2 respectively), so based on intensive parameters, the upper layer can be also identified as smoke.

1 April 2021: Dust

Dust layers transported from Africa are regularly observed over North of France. One such dust episode took place in the night 1-2 April 2021 and the corresponding spatio-temporal variations of β_{532}, β_F, δ_{532}, and G_F are shown in Fig.17. The dust layer, with depolarization ratio exceeding 30%, and low fluorescence, extends from approximately 1.0 km to 5.0 km height. The fluorescence capacity varied inside the layer. In the center it was the lowest (about 0.1×10^{-4}), but at the bottom of the layer and near the top, G_F increased up to $(0.2\div0.3)\times10^{-4}$. In Fig.18a, ($\delta_{532}$-$G_F$ diagram), we observe a cluster of particles, which can be identified as dust. There is also a second small cluster, attributed to urban aerosols. On the distribution of particle types in Fig.18b the urban aerosol occurs below 800 m after 23:00 UTC.

Fig.19 provides vertical profiles of β_{532}, δ_{532}, δ_{355}, β_F, G_F and $A^{\beta}_{355/532}$. Measurements at 1064 nm were not available for this episode. Depolarization ratios at 355 nm and 532 nm are close to 30% through the layer, though at heights below 1.5 km there is small enhancement of δ_{532} up to 34%. The fluorescence capacity is about 0.4×10^{-4} at 1.5 km and it decreases with height to 0.1×10^{-4} at 2.5 km. However, this decrease is not accompanied by changes in depolarization ratio. The backscattering Ångstrom exponent $A^{\beta}_{355/532}$ is sensitive to the enhancement of dust absorption in UV and can be negative (Veselovskii et al., 2020a). For this episode $A^{\beta}_{355/532}$ decreases with height (together with G_F) to -0.3 at 2.5 km. Similar values of $A^{\beta}_{355/532}$ were observed during SHADOW campaign in Western Sahara (Veselovskii et al., 2020a). Above 3.75 km both $A^{\beta}_{355/532}$ and G_F start to increase. Hence, dust properties change with height and this change is not revealed on δ_{532}

profile. We should mention, that in publication of Veselovskii et al. (2020a), increase of the dust imaginary part in UV also did not lead to changes in δ_{532}.

Application of our new "Fluorescence – Depolarization" based approach to six episodes considered in this section, demonstrates its ability to discriminate several aerosol types. The first step in validation of the results presented, could be comparison of the particle properties for obtained aerosol types with corresponding values, used in existing typing algorithms. Table 3 provides the range of variation of particle intensive properties from publications of Burton et al., (2013), synthetic values used in NATALI algorithm (Nicolae et al., 2018) and parameters used in the algorithm of Papagiannopoulos et al. (2018) for the urban, smoke and dust particles. The table contains also the range of properties variation for the episodes considered in current study for the same aerosol types. Parameters chosen in different algorithms, even for the same aerosol type, vary in a wide range, and the values observed in this study mainly match this range of variation. We observe higher values of $A^{\beta}_{355/532}$ for urban and smoke particles, and for dust, $A^{\beta}_{355/532}$ could be negative. Still, the values obtained in this study and the values used by other algorithms are in reasonable agreement.

Conclusion

The results presented in this study can be considered as the first important step in the combination of Mie – Raman and fluorescence lidar data. In approach presented, only two intensive parameters are used for classification: the particle depolarization ratio δ_{532} and the fluorescence capacity G_F. These parameters are chosen because they are specific for different types of aerosol and can be calculated with high spatio-temporal resolution. Moreover, δ_{532} and G_F can be calculated at lower altitudes, compared to extinction related parameters, such as lidar ratio and extinction Angstrom exponent. Thus classification, in principle, is possible at ranges with incomplete geometrical overlap. Finally, computation of β_F does not demand the use of reference height, only calibration of relative sensitivity of the channels is needed. Thus, aerosol classification is possible, even in the presence of low-level clouds.

Though only two aerosol properties are considered, the use of fluorescence provides advances in aerosol classification. Analysis of numerous observations, performed at Lille University for the period 2020 – 2021, demonstrates the possibility to separate four types of aerosols, such as dust, smoke, pollen and urban. Moreover, we are able to identify the layers

554 containing the liquid water particles and ice. The number of determined aerosol classes can be
555 increased, by considering the particle mixtures. In particular, “pure” dust can be considered
556 separately from “polluted” one, which can be discriminated by lower values of the depolarization
557 ratio.

558 Fluorescence technique is especially promising for separation of smoke and urban particles,
559 because fluorescence capacity of smoke is about factor five higher. The important advantage of
560 fluorescence measurements is the ability to identify the biological particles in the atmosphere, such
561 as pollen, which are usually not included in the classification schemes, based on Mie-Raman
562 observations. At the same time, our observations demonstrate that biological particles are
563 frequently observed during Spring – Autumn seasons and may contribute significantly to the
564 aerosol composition inside the PBL. The developed approach allows to identify aerosol types with
565 high spatio-temporal resolutions, which is estimated to be 60 m for height and less than 10 minutes
566 for time, for the current instrumental configuration. Such resolution provides an opportunity for
567 investigating the dynamics of aerosol mixing in the troposphere.

568 The next step in algorithm development will be to include additional particle properties.
569 We plan to include the backscattering Angstrom exponents and the depolarization spectral ratios
570 ($\delta_{355}/\delta_{532}$ and $\delta_{532}/\delta_{1064}$), which can be also calculated with high spatio-temporal resolutions. The
571 fluorescence capacity depends on the relative humidity, due to the effects of hygroscopic growth.
572 Thus, information about spatio-temporal distribution of RH should be included in the analysis. It
573 is also important to combine our algorithm with existing classification schemes, which we plan to
574 consider in the near future.

575

576 ***Data availability***. Lidar measurements are available upon request
577 (philippe.goloub@univ-lille.fr).
578
579 ***Author contributions***. IV processed the data and wrote the paper. QH and TP performed the
580 measurements. PG supervised the project and helped with paper preparation. BB prepared
581 algorithm for aerosol classification. MK developed software for data processing.
582 .

583 ***Competing interests***. The authors declare that they have no conflict of interests.

584

585 **Acknowledgement**

We acknowledge funding from the CaPPA project funded by the ANR through the PIA under contract ANR-11-LABX-0005-01, the "Hauts de France" Regional Council (project CLIMIBIO) and the European Regional Development Fund (FEDER). ESA/QA4EO program is greatly acknowledged for support of observation activity at LOA as well as OBS4CLIM Equipex project funded by ANR. Development of algorithm for aerosol typing was supported by Russian Science Foundation (project 21-17-00114). The SILAM model is acknowledged for providing pollen simulations.

References

Adam, M., Stachlewska, I. S., Mona, L., Papagiannopoulos, N., Bravo-Aranda, J. A., Sicard, M., Nicolae, D. N., Belegante, L., Janicka, L., Szczepanik, D., Mylonaki, M., Papanikolaou, C.-A., Siomos, N., Voudouri, K. A., Alados-Arboledas, L., Apituley, A., Mattis, I., Chaikovsky, A., Muñoz-Porcar, C., Pietruczuk, A., Bortoli, D., Baars, H., Grigorov, I., and Peshev, Z.: Biomass burning events measured by lidars in EARLINET – Part 2: Optical properties investigation, Atmos. Chem. Phys. Discuss., https://doi.org/10.5194/acp-2021-759, in review, 2021.

Ansmann, A., Riebesell, M., Wandinger, U., Weitkamp, C., Voss, E., Lahmann, W., and Michaelis, W.: Combined Raman elastic-backscatter lidar for vertical profiling of moisture, aerosols extinction, backscatter, and lidar ratio, Appl.Phys.B, *55*, 18-28, 1992.

Bohlmann, S., Shang, X., Giannakaki, E., Filioglou, M., Saarto, A., Romakkaniemi, S. and Komppula, M.: Detection and characterization of birch pollen in the atmosphere using multi-wavelength Raman lidar in Finland, Atmos. Chem. Phys. 19, 14559–14569, 2019. doi.org/10.5194/acp-19-14559-2019.

Boucher, O., Randall, D., Artaxo, P., Bretherton, C., Feingold, G., Forster, P., Kerminen, V.-M., Kondo, Y., Liao, H., Lohmann, U., Rasch, P., Satheesh, S. K., Sherwood, S., Stevens, B., and Zhang, X. Y.: Clouds and Aerosols, in: Climate Change 2013: The Physical Science Basis. Contribution of Working Group I to the Fifth Assessment Report of the Intergovernmental Panel on Climate Change, edited by: Stocker, T. F., Qin, D., Plattner, G.-K., Tignor, M., Allen, S. K., Boschung, J., Nauels, A., Xia, Y., Bex, V., and Midgley, P., M., Cambridge University Press, Cambridge, United Kingdom and New York, NY, USA, 2013

Burton, S. P., Ferrare, R. A., Hostetler, C. A., Hair, J.W., Rogers, R. R., Obland, M. D., Butler, C. F., Cook, A. L., Harper, D. B., and Froyd, K. D.: Aerosol classification using airborne High

Spectral Resolution Lidar measurements – methodology and examples, Atmos. Meas. Tech., 5, 73–98, 2012. https://doi.org/10.5194/amt-5-73-2012

Burton, S. P., Ferrare, R. A., Vaughan, M. A., Omar, A. H., Rogers, R. R., Hostetler, C. A., and Hair, J. W.: Aerosol classification from airborne HSRL and comparisons with the CALIPSO vertical feature mask, Atmos. Meas. Tech., 6, 1397–1412, 2013. https://doi.org/10.5194/amt-6-1397-2013

Burton, S. P., Vaughan, M. A., Ferrare, R. A. and Hostetler, C. A.: Separating mixtures of aerosol types in airborne High Spectral Resolution Lidar data. Atmos. Meas. Tech. 7, 419-436, 2014. DOI: 10.5194/amt-7-419-2014

Burton, S. P., Hair, J. W., Kahnert, M., Ferrare, R. A., Hostetler, C. A., Cook, A. L., Harper, D. B., Berkoff, T. A., Seaman, S. T., Collins, J. E., Fenn, M. A., and Rogers, R. R.: Observations of the spectral dependence of linear particle depolarization ratio of aerosols using NASA Langley airborne High Spectral Resolution Lidar, Atmos. Chem. Phys., 15, 13453–13473, 2015 doi:10.5194/acp-15-13453-2015

Cao, X., Roy, G., and Bernier, R.: Lidar polarization discrimination of bioaerosols, Opt. Eng., 49, 116201, https://doi.org/10.1117/1.3505877, 2010.

Dubovik, O., Holben, B. N., Eck, T. F., Smirnov, A., Kaufman, Y. J., King, M. D., Tanre, D., and Slutsker, I.: Variability of absorption and optical properties of key aerosol types observed in worldwide locations, J. Atmos. Sci., 59, 590–608, 2002.

Freudenthaler,V., Esselborn, M.,Wiegner, M.,Heese, B., Tesche, M. and co-authors: Depolarization ratio profiling at several wavelengths in pure Saharan dust during SAMUM 2006, *Tellus* 61B, 165–179, 2009.

Gasteiger, J. and Freudenthaler, V.: Benefit of depolarization ratio at $\lambda = 1064$ nm for the retrieval of the aerosol microphysics from lidar measurements. Atmos. Meas. Tech. 7, 3773-3781, 2014. DOI: 10.5194/amt-7-3773-2014

Giles, D. M., Holben, B. N., Eck, T. F., Sinyuk, A., Smirnov, A., Slutsker, I., Dickerson, R. R., Thompson, A. M., and Schafer, J. S.: An analysis of AERONET aerosol absorption properties and classifications representative of aerosol source regions, J. Geophys. Res. 117, D17203, https://doi.org/10.1029/2012JD018127, 2012.

Groß, S., Tesche, M., Freudenthaler, V., Toledano, C., Wiegner, M., Ansmann, A., Althausen D., Seefeldner, M.:. Characterization of Saharan dust, marine aerosols and mixtures of biomass-

burning aerosols and dust by means of multi-wavelength depolarization and Raman lidar measurements during SAMUM 2. Tellus B 63, 706-724, 2011. DOI: 10.1111/j.1600-0889.2011.00556.

Groß, S., Esselborn, M., Weinzierl, B., Wirth, M., Fix, A., and Petzold, A.: Aerosol classification by airborne high spectral resolution lidar observations, Atmos. Chem. Phys., 13, 2487–2505, 2013. https://doi.org/10.5194/acp-13-2487-2013

Haarig, M., Ansmann, A., Baars, H., Jimenez, C., Veselovskii, I., Engelmann, R., and Althausen, D.: Depolarization and lidar ratios at 355, 532, and 1064 nm and microphysical properties of aged tropospheric and stratospheric Canadian wildfire smoke, Atmospheric Chemistry and Physics, 18, 11 847–11 861, 2018.

Hamill, P., Giordano, M., Ward, C., Giles, D., and Holben, B.: An AERONET-based aerosol classification using the Mahalanobis distance, Atmos. Environ., 140, 213–233, https://doi.org/10.1016/j.atmosenv.2016.06.002, 2016.

Hara, Y., Nishizawa, T., Sugimoto , N., Osada, K., Yumimoto, K., Uno, I., Kudo, R., and Ishimoto, H.: Retrieval of aerosol components using multi-wavelength Mie-Raman lidar and comparison with ground aerosol sampling, Remote Sens., 10, 937, 2018. https://doi:10.3390/rs10060937

Hu, Q., Goloub, P., Veselovskii, I., Bravo-Aranda, J.-A., Popovici, I. E., Podvin, T., Haeffelin, M., Lopatin, A., Dubovik, O., Pietras, C., et al.: Long-range-transported Canadian smoke plumes in the lower stratosphere over northern France, Atmospheric Chemistry and Physics, 19, 1173–1193, 2019.

Hu, Q., Goloub, P., Veselovskii, I., and Podvin, T.: The characterization of long-range transported North American biomass burning plumes: what can a multi-wavelength Mie-Raman-polarization-fluorescence lidar provide?, Atmos. Chem. Phys., 22, 5399–5414, 2022 https://doi.org/10.5194/acp-22-5399-2022

HYSPLIT(2022): HYbrid Single-Particle Lagrangian Integrated Trajectory model, backward trajectory calculation tool, available at: http://ready.arl.noaa.gov/HYSPLIT_traj.php, last access: 14 June 2022.

Klett J.D., “Lidar inversion with variable backscatter/extinction ratios”, Appl.Opt. 24, 1638-1643, 1985.

Li, L., Dubovik, O., Derimian, Y., Schuster, G. L., Lapyonok, T., Litvinov, P., Ducos, F., Fuertes, D., Chen, C., Li, Z., Lopatin, A., Torres, B., and Che, H.: Retrieval of aerosol components

directly from satellite and ground-based measurements, Atmos. Chem. Phys., 19, 13409–13443, 2019. https://doi.org/10.5194/acp-19-13409-2019

Mamouri, R.-E., and Ansmann, A.: Potential of polarization/Raman lidar to separate fine dust, coarse dust, maritime, and anthropogenic aerosol profiles, Atmos. Meas. Tech., 10, 3403–3427, 2017. https://doi.org/10.5194/amt-10-3403-2017

Müller, D., Mattis, I., Wandinger, U., Ansmann, A., Althausen, A., and Stohl, A.: Raman lidar observations of aged Siberian and Canadian forest fire smoke in the free troposphere over Germany in 2003: Microphysical particle characterization, J. Geophys. Res., 110, D17201, doi:10.1029/2004JD005756, 2005.

Mylonaki, M., Giannakaki, E., Papayannis, A., Papanikolaou, C.-A., Komppula, M., Nicolae, D., Papagiannopoulos, N., Amodeo, A., Baars, H., and Soupiona, O.: Aerosol type classification analysis using EARLINET multiwavelength and depolarization lidar observations, Atmos. Chem. Phys., 21, 2211–2227, 2021. https://doi.org/10.5194/acp-21-2211-2021

Nicolae, D., Vasilescu, J., Talianu, C., Binietoglou, I., Nicolae, V., Andrei, S., and Antonescu, B.: A neural network aerosol-typing algorithm based on lidar data, Atmos. Chem. Phys., 18, 14511–14537, 2018. https://doi.org/10.5194/acp-18-14511-2018

Papagiannopoulos, N., Mona, L., Amodeo, A., D'Amico, G., Gumà Claramunt, P., Pappalardo, G., Alados-Arboledas, L., Guerrero- Rascado, J. L., Amiridis, V., Kokkalis, P., Apituley, A., Baars, H., Schwarz, A.,Wandinger, U., Binietoglou, I., Nicolae, D., Bortoli, D., Comerón, A., Rodríguez-Gómez, A., Sicard, M., Papayannis, A., and Wiegner, M.: An automatic observation-based aerosol typing method for EARLINET, Atmos. Chem. Phys., 18, 15879– 15901, 2018. https://doi.org/10.5194/acp-18-15879-2018

Pappalardo, G., Amodeo, A., Apituley, A., Comeron, A., Freudenthaler, V., Linné, H., Ansmann, A., Bösenberg, J., D'Amico, G., Mattis, I., Mona, L., Wandinger, U., Amiridis, V., Alados-Arboledas, L., Nicolae, D., and Wiegner, M.: EARLINET: towards an advanced sustainable European aerosol lidar network, Atmos. Meas. Tech., 7, 2389–2409, 2014. https://doi.org/10.5194/amt- 7-2389-2014, 2014.

Reichardt, J., Leinweber, R., Schwebe, A.: Fluorescing aerosols and clouds: investigations of co-existence, Proceedings of the 28th ILRC, Bucharest, Romania, 25-30 June, 2017.

Rittmeister, F., Ansmann, A., Engelmann, R., Skupin, A., Baars, H., Kanitz, T., and Kinne, S.: Profiling of Saharan dust from the Caribbean to western Africa –Part 1: Layering structures and

optical properties from shipborne polarization/Raman lidar observations, Atmos. Chem. Phys., 17, 12963–12983, 2017. https://doi.org/10.5194/acp-17-12963-2017

Saito,Y., Hosokawa, T., Shiraishi, K.: Collection of excitation-emission-matrix fluorescence of aerosol-candidate-substances and its application to fluorescence lidar monitoring, Appl. Opt., 61, 653 – 660, 2022.

Schuster, G. L., Dubovik, O., and Arola, A.: Remote sensing of soot carbon – Part 1: Distinguishing different absorbing aerosol species, Atmos. Chem. Phys., 16, 1565–1585, https://doi.org/10.5194/acp-16-1565-2016, 2016.

Sicard, M., Fortunato dos Santos Oliveira, D. C., Muñoz-Porcar, C., Gil-Díaz, C., Comerón, A., Rodríguez-Gómez, A., and Dios Otín, F.: Measurement Report: Spectral and statistical analysis of aerosol hygroscopic growth from multi-wavelength lidar measurements in Barcelona, Spain, Atmos. Chem. Phys. 22, 7681–7697, 2022. https://doi.org/10.5194/acp-22-7681-2022

Sofiev, M., Siljamo, P., Ranta, H., Linkosalo, T., Jaeger,S., Rasmussen, A., Rantio-Lehtimaki, A., Severova, E., Kukkonen, J. (2012) A numerical model of birch pollen emission and dispersion in the atmosphere. Description of the emission module. Int.J.Biometeorology, http://www.ncbi.nlm.nih.gov/pubmed/22410824, DOI 10.1007/s00484-012-0532-z, PMID 22410824

Sofiev, M., Vira, J., Kouznetsov, R., Prank, M., Soares, J., Genikhovich, E. (2015) Construction of the SILAM Eulerian atmospheric dispersion model based on the advection algorithm of Michael Galperin, Geosci.Model Developm. 8, 3497-3522, doi:10.5194/gmd-8-3497-2015

Sofiev, M. On impact of transport conditions on variability of the seasonal pollen index. Aerobiologia 33, 167–179 (2017). https://doi.org/10.1007/s10453-016-9459-x

Sugimoto, N. and Lee, C. H.: Characteristics of dust aerosols inferred from lidar depolarization measurements at two wavelengths. Applied Optics 45, 7468-7474, 2006. DOI: 10.1364/AO.45.007468

Sugimoto, N., Huang, Z., Nishizawa, T., Matsui, I., Tatarov, B.: Fluorescence from atmospheric aerosols observed with a multichannel lidar spectrometer," Opt. Expr. 20, 20800-20807, 2012.

Tesche, M., Ansmann, A., Müller, D., Althausen, D., Mattis, I., Heese, B., Freudenthaler, V., Wiegner, M., Eseelborn, M., Pisani, G., and Knippertz, P.: Vertical profiling of Saharan dust with Raman lidars and airborne HSRL in southern Morocco during SAMUM, Tellus B, 61, 144–164, 2009.

741 Veselovskii, I., Whiteman, D. N., Korenskiy, M., Suvorina, A., Perez-Ramirez, D.: Use of
742 rotational Raman measurements in multiwavelength aerosol lidar for evaluation of particle
743 backscattering and extinction, Atmos. Meas. Tech., 8, 4111–4122, 2015.
744 Veselovskii, I., Hu, Q., Goloub, P., Podvin, T., Korenskiy, M., Derimian, Y., Legrand, M., and
745 Castellanos, P.: Variability in lidar-derived particle properties over West Africa due to changes
746 in absorption: towards an understanding, Atmos. Chem. Phys., 20, 6563–6581, 2020a.
747 https://doi.org/10.5194/acp-20-6563-2020a
748 Veselovskii, I., Hu, Q., Goloub, P., Podvin, T., Korenskiy, M., Pujol, O., Dubovik, O., Lopatin,
749 A.: Combined use of Mie-Raman and fluorescence lidar observations for improving aerosol
750 characterization: feasibility experiment, Atm. Meas. Tech., 13, 6691–6701, 2020b.
751 doi.org/10.5194/amt-13-6691-2020.
752 Veselovskii, I., Hu, Q., Goloub, P., Podvin, T., Choël, M., Visez, N., and Korenskiy, M.: Mie–
753 Raman–fluorescence lidar observations of aerosols during pollen season in the north of France,
754 Atm. Meas. Tech., 14, 4773–4786, 2021. doi.org/10.5194/amt-14-4773-2021
755 Veselovskii, I., Hu, Q., Ansmann, A., Goloub, P., Podvin, T., Korenskiy, N.: Fluorescence lidar
756 observations of wildfire smoke inside cirrus: A contribution to smoke-cirrus - interaction
757 research, Atmos. Chem. Phys. 22, 5209–5221, 2022. https://doi.org/10.5194/acp-22-5209-2022
758 Voudouri, K. A., Siomos, N., Michailidis, K., Papagiannopoulos, N., Mona, L., Cornacchia, C.,
759 Nicolae, D., and Balis, D.: Comparison of two automated aerosol typing methods and their
760 application to an EARLINET station, Atmos. Chem. Phys., 19, 10961–10980, 2019.
761 https://doi.org/10.5194/acp-19-10961-2019
762 Wang, N., Shen, X., Xiao, D., Veselovskii, I., Zhao,C., Chen, F., Liu, C., Rong, Y., Ke, J., Wang,
763 B., Qi, B., Liu, D.: Development of ZJU high-spectral-resolution lidar for aerosol and cloud:
764 feature detection and classification, Journal of Quantitative Spectroscopy & Radiative Transfer,
765 v.261, 107513, 2021. doi.org/10.1016/j.jqsrt.2021.107513
766 Whiteman, D.N.: Examination of the traditional Raman lidar technique. II. Evaluating the ratios
767 for water vapor and aerosols, Appl. Opt., 42, 2593-2608, 2003.
768 https://doi.org/10.1364/AO.42.002593
769 Zhang, Y., Li, Z., Chen, Y., Leeuw, G., Zhang, C., Xie, Y., and Li, K.: Improved inversion of
770 aerosol components in the atmospheric column from remote sensing data, Atmos. Chem. Phys.,
771 20, 12795–12811, 2020. https://doi.org/10.5194/acp-20-12795-2020

Zhang, Y., Sun, Z., Chen, S., Chen, H., Guo, P., Chen, S., He, J., Wang, J., Nian, X.: Classification and source analysis of low-altitude aerosols in Beijing using fluorescence–Mie polarization lidar, Optics Communications, 479, 126417, 2021. https://doi.org/10.1016/j.optcom.2020.126417

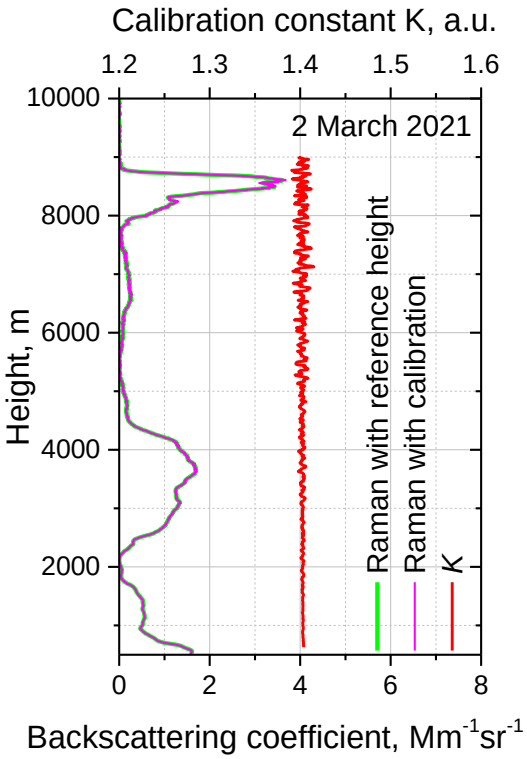

Fig.1. Backscattering coefficients at 532 nm for period 19:00 – 20:00 UTC on 2 March 2021 calculated from Mie-Raman observations using the reference height as Ansmann et al. (1992) (green) or the calibration constant as in Eq 5. (magenta). The profile of calibration constant *K* is shown with red line.

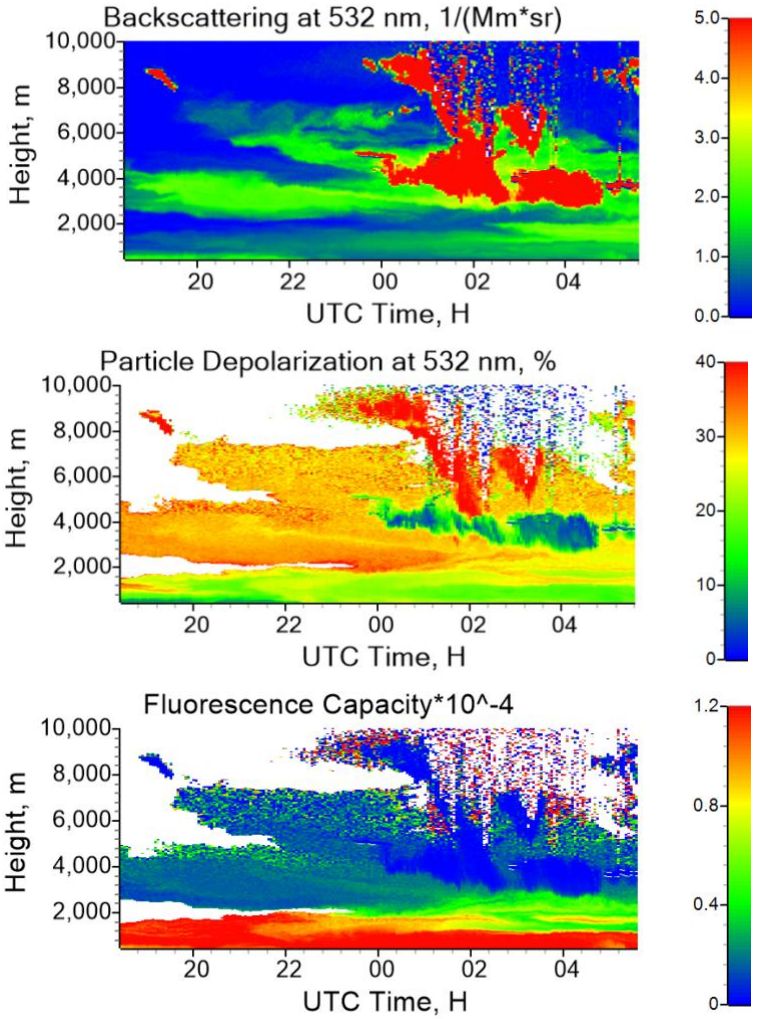

Fig.2. Spatio-temporal distributions of the backscattering coefficient β_{532}, the particle depolarization ratio δ_{532} and the fluorescence capacity G_F in the night 2-3 March 2021. The backscattering coefficient β_{532} is calculated with the modified Raman method. The values of δ_{532}, and G_F are shown for $\beta_{532}>0.2$ $Mm^{-1}sr^{-1}$.

797

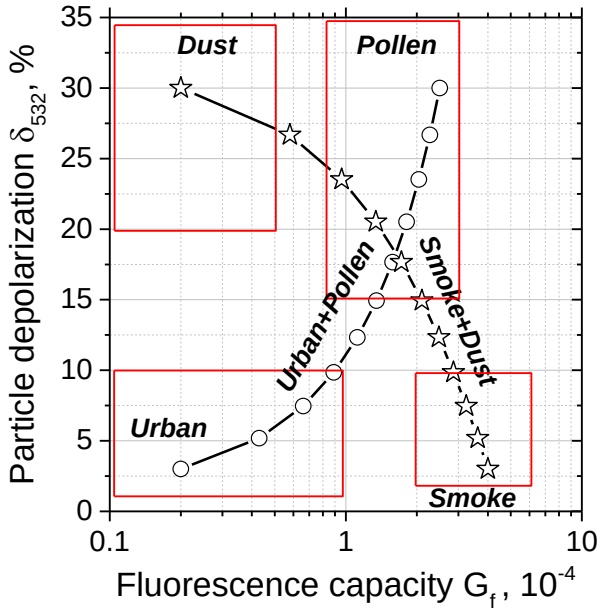

798

799 Fig.3. Aerosol typing with δ_{532}-G_F diagram. The ranges of the particle parameters variation for
800 dust, pollen, smoke and urban aerosol are given by rectangles. The symbols show the results of
801 simulation performed for pollen+urban (circles) and smoke + dust (stars) mixtures. Relative
802 contribution of pollen (smoke) to the total backscattering β_{532} varied in 0 – 1.0 range with step 0.1.
803 Particle parameters used in calculations are given in the text.

804

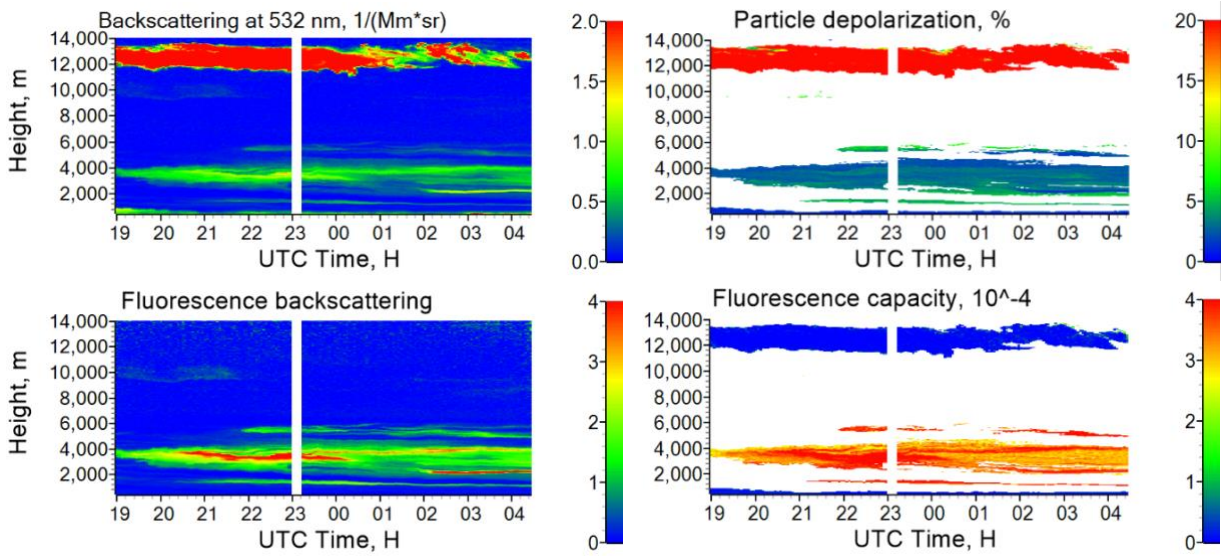

Fig.4. Spatio-temporal distributions of the backscattering coefficient β_{532}, the fluorescence backscattering coefficient β_F (in 10^{-4} $Mm^{-1}sr^{-1}$), the particle depolarization ratio δ_{532}; and the fluorescence capacity G_F in the night 12-13 September 2020. Calculation of δ_{532} and G_F was not performed for β_{532}<0.2 $Mm^{-1}sr^{-1}$. The values of backscattering coefficient and depolarization ratio of ice clouds are high (above 20 $Mm^{-1}sr^{-1}$ and 40% respectively) and are off scale on the maps presented.

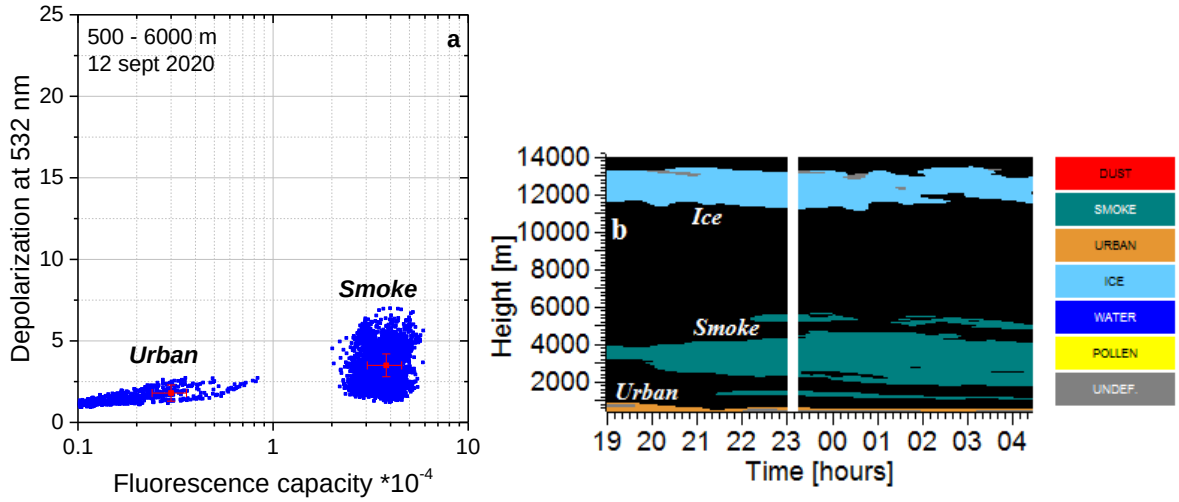

Fig.5 (a) The δ_{532}-G_F diagram for data from Fig.4 in 500 – 6000 m height range, red crosses show the uncertainty of the measurements. (b) Spatio-temporal distribution of aerosol types in the night 12-13 September 2020. Grey color shows undefined aerosol type, while measurements with β_{532}<0.2 $Mm^{-1}sr^{-1}$ are marked by black color.

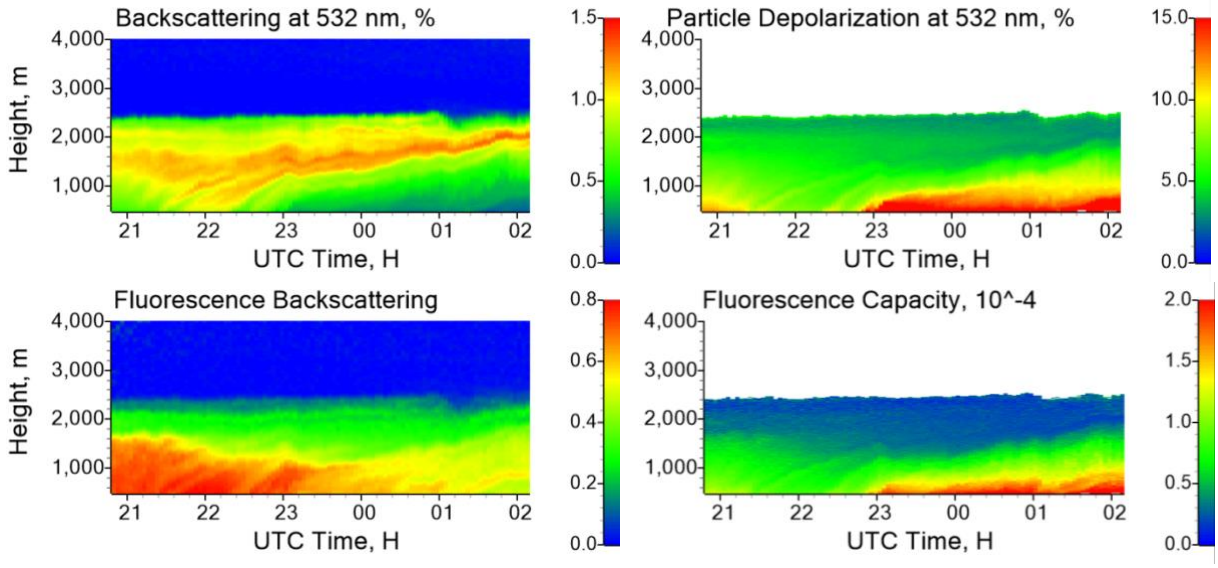

Fig.6. Spatio-temporal distributions of the backscattering coefficient β_{532}; the fluorescence backscattering coefficient β_F (in 10^{-4} $Mm^{-1}sr^{-1}$); the particle depolarization ratio δ_{532}; and the fluorescence capacity G_F in the night 30-31 May 2020. The values of δ_{532}, and G_F are shown for β_{532}>0.2 $Mm^{-1}sr^{-1}$.

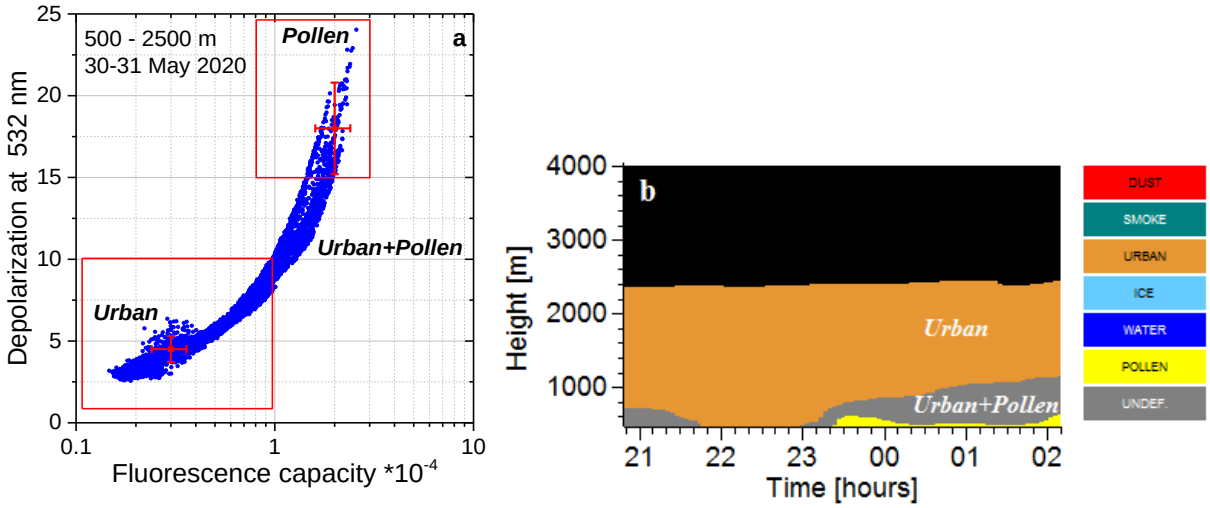

Fig.7. (a) The δ_{532}-G_F diagram for observations in 500 m – 2500 m height range and (b) spatio-temporal distribution of aerosol types on the night 30-31 May 2020. Grey color shows undefined aerosol type, which is a mixture of urban and pollen for this case. Measurements with β_{532}<0.2 $Mm^{-1}sr^{-1}$ are marked by black color.

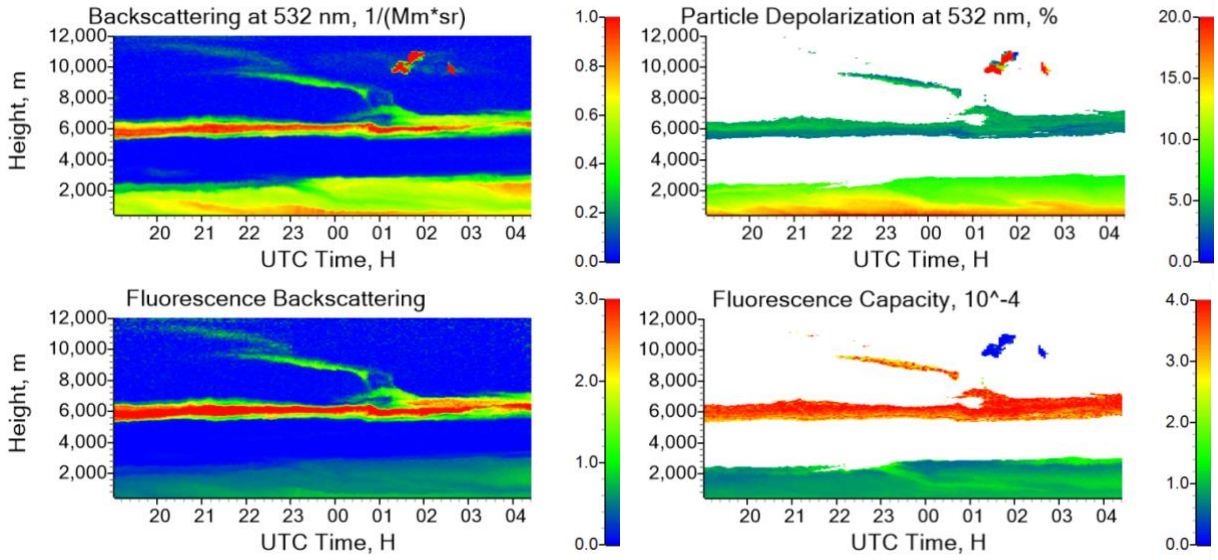

Fig.8. Spatio-temporal distributions of the backscattering coefficient β_{532}, the fluorescence backscattering coefficient β_F (in 10^{-4} $Mm^{-1}sr^{-1}$), the particle depolarization ratio δ_{532}, and the fluorescence capacity G_F in the night 14 – 15 September 2020. The values of δ_{532}, and G_F are shown for $\beta_{532}>0.2$ $Mm^{-1}sr^{-1}$.

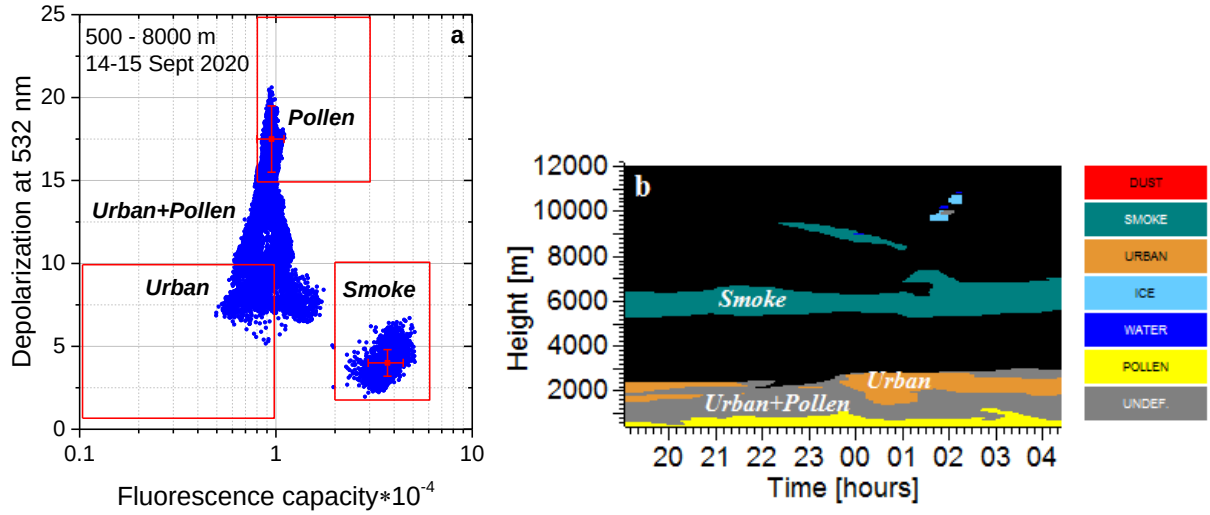

Fig.9. (a) The δ_{532}-G_F diagram for observations in 500 m – 8000 m height range and (b) spatio-temporal distribution of aerosol types in the night 14 – 15 September 2020. Grey color shows undefined aerosol type, which is a mixture of pollen, urban and smoke particles. Measurements with $\beta_{532}<0.2$ $Mm^{-1}sr^{-1}$ are marked by black color.

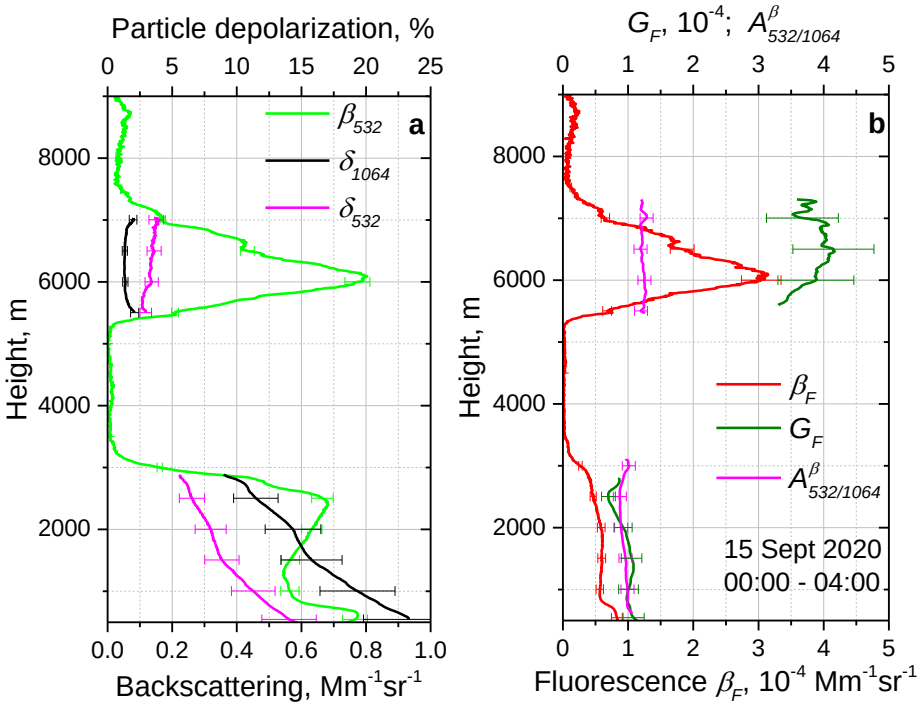

Fig.10. Vertical profiles of (a) backscattering coefficient β_{532} and particle depolarization ratios δ_{532}, δ_{1064}; (b) fluorescence backscattering β_F, fluorescence capacity G_F and backscattering Angstrom exponent $A^{\beta}_{532/1064}$ on 15 September 2020 for period 00:00 – 04:00 UTC.

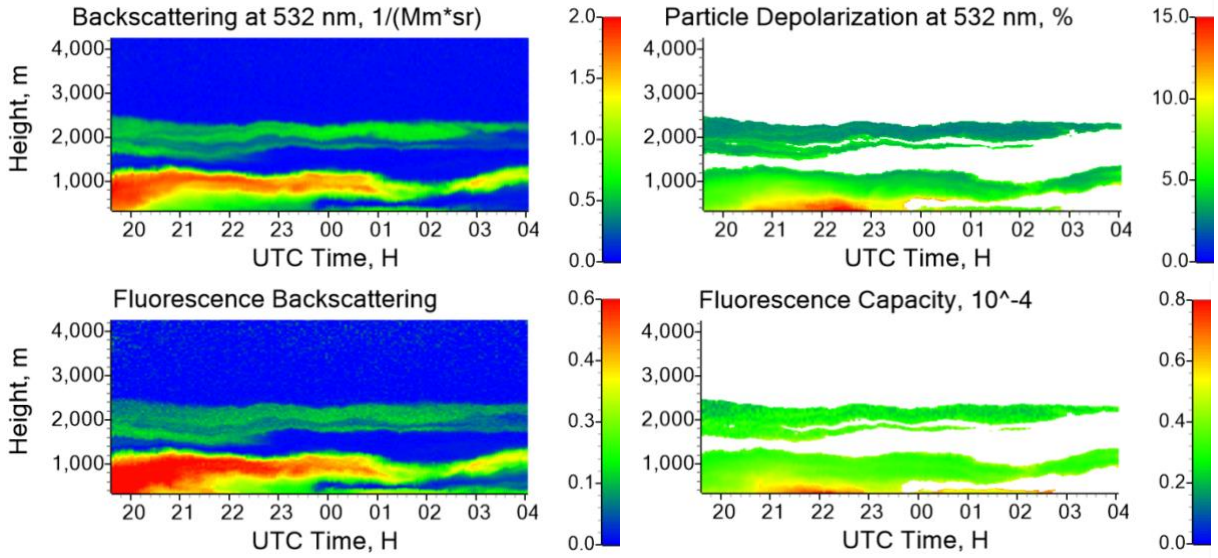

Fig.11. Spatio-temporal distributions of the backscattering coefficient β_{532}, the fluorescence backscattering coefficient β_F (in 10^{-4} $Mm^{-1}sr^{-1}$), the particle depolarization ratio δ_{532}; and the fluorescence capacity G_F in the night 10 – 11 April 2020. Measurements are performed at an angle of 45 dg to horizon. The values of δ_{532}, and G_F are shown for β_{532}>0.2 $Mm^{-1}sr^{-1}$.

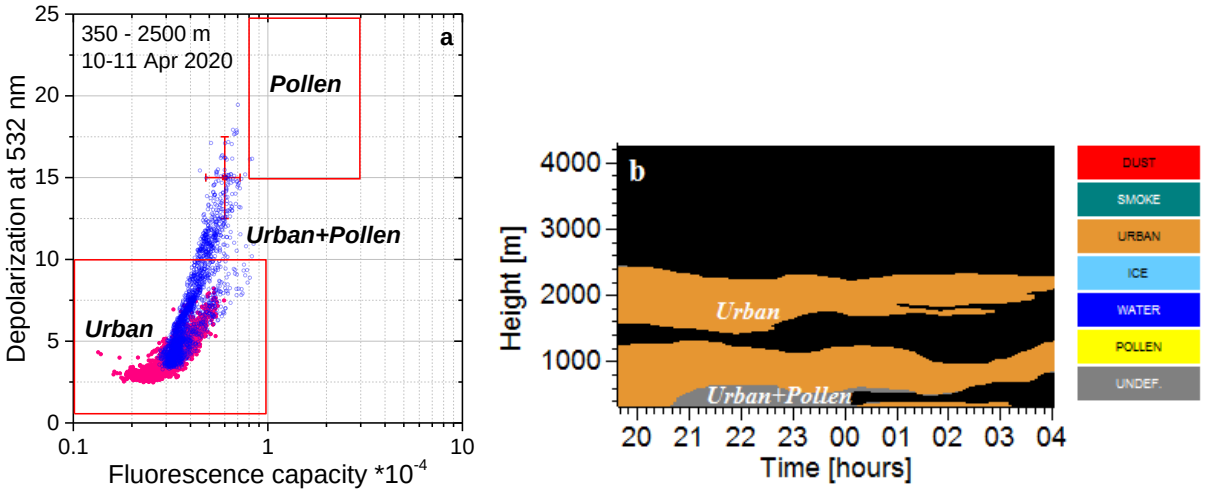

Fig.12. (a) The δ_{532}-G_F diagram for observations in 350 – 1500 m (blue symbols) and 1500 – 2500 m (pink symbols) height ranges. (b) Spatio-temporal distribution of aerosol types in the night 10 – 11 April 2020. Grey color shows undefined aerosol type, which is a mixture of urban and pollen for this case. Measurements with β_{532}<0.2 $Mm^{-1}sr^{-1}$ are marked by black color.

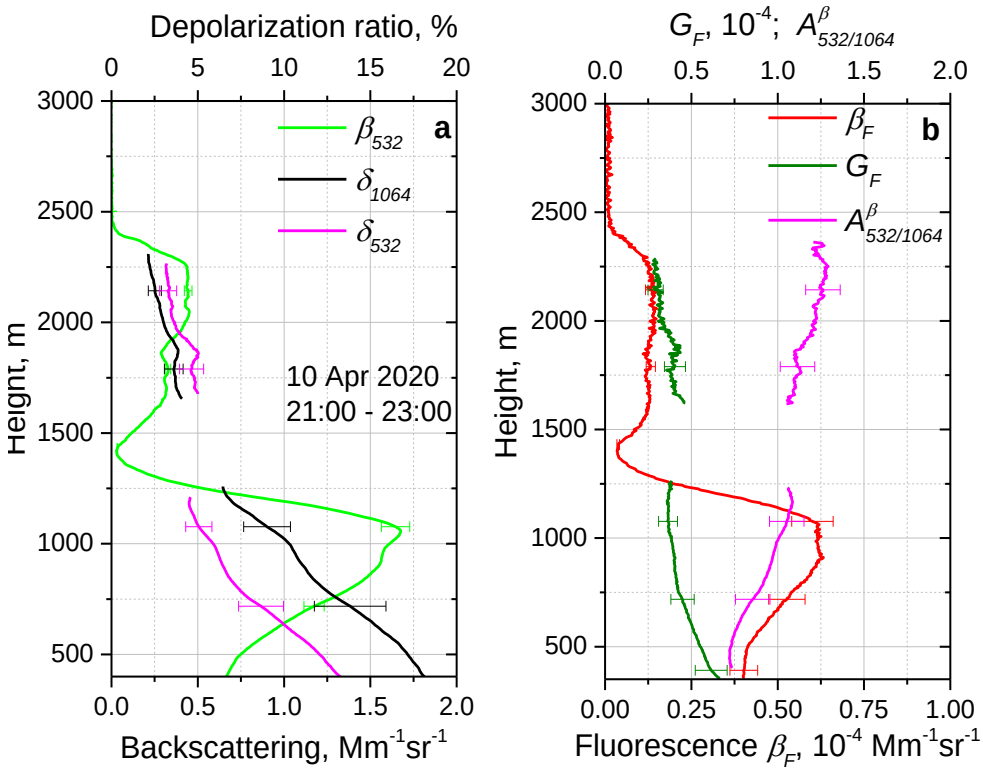

878
879 Fig.13. Vertical profiles of (a) backscattering coefficient β_{532} and particle depolarization ratios δ_{532},
880 δ_{1064}; (b) fluorescence backscattering β_F, fluorescence capacity G_F and backscattering Angstrom
881 exponent $A^{\beta}_{532/1064}$ on 10 April 2020 for period 21:00 – 23:00 UTC.
882

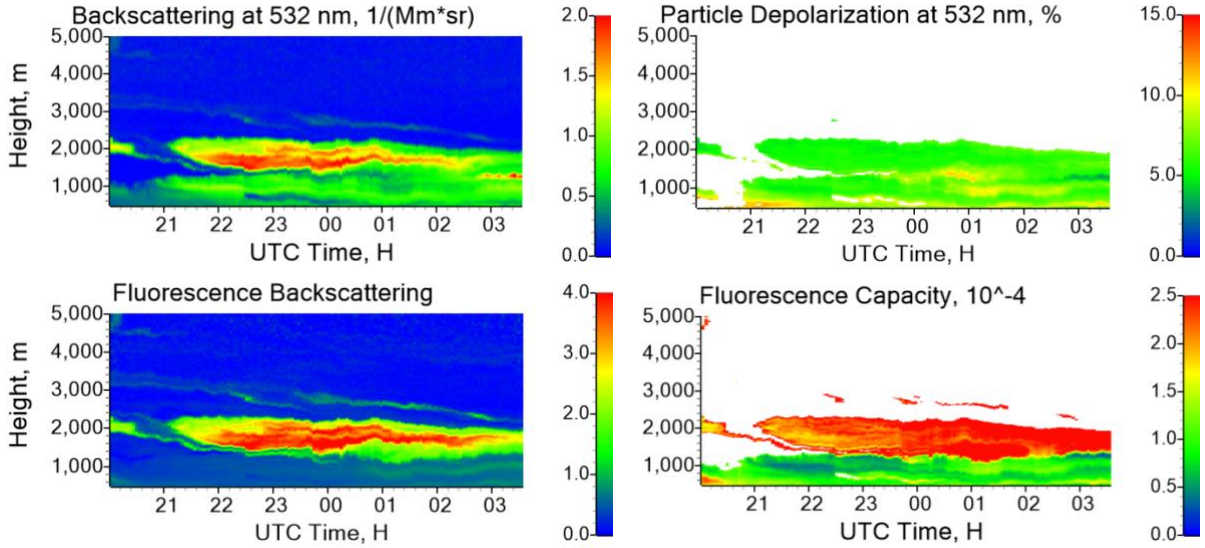

Fig.14. Spatio-temporal distributions of the backscattering coefficient β_{532}, the fluorescence backscattering coefficient β_F (in 10^{-4} $Mm^{-1}sr^{-1}$), the particle depolarization ratio δ_{532}, and the fluorescence capacity G_F in the night 11 – 12 August 2021. The values of δ_{532}, and G_F are shown for $\beta_{532}>0.3$ $Mm^{-1}sr^{-1}$.

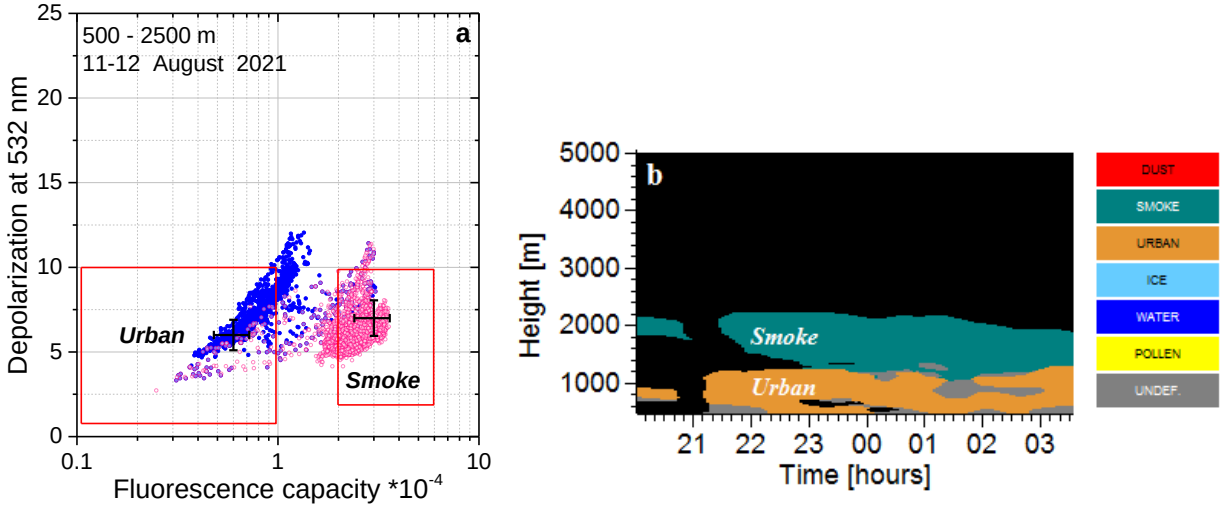

Fig.15. (a) The δ_{532}-G_F diagram for observations in 500 – 1400 m (blue symbols) and 1400 – 2500 m (pink symbols) height ranges. (b) Spatio-temporal distribution of aerosol types in the night 11-12 August 2021. Measurements with $\beta_{532}<0.3$ $Mm^{-1}sr^{-1}$ are marked by black color.

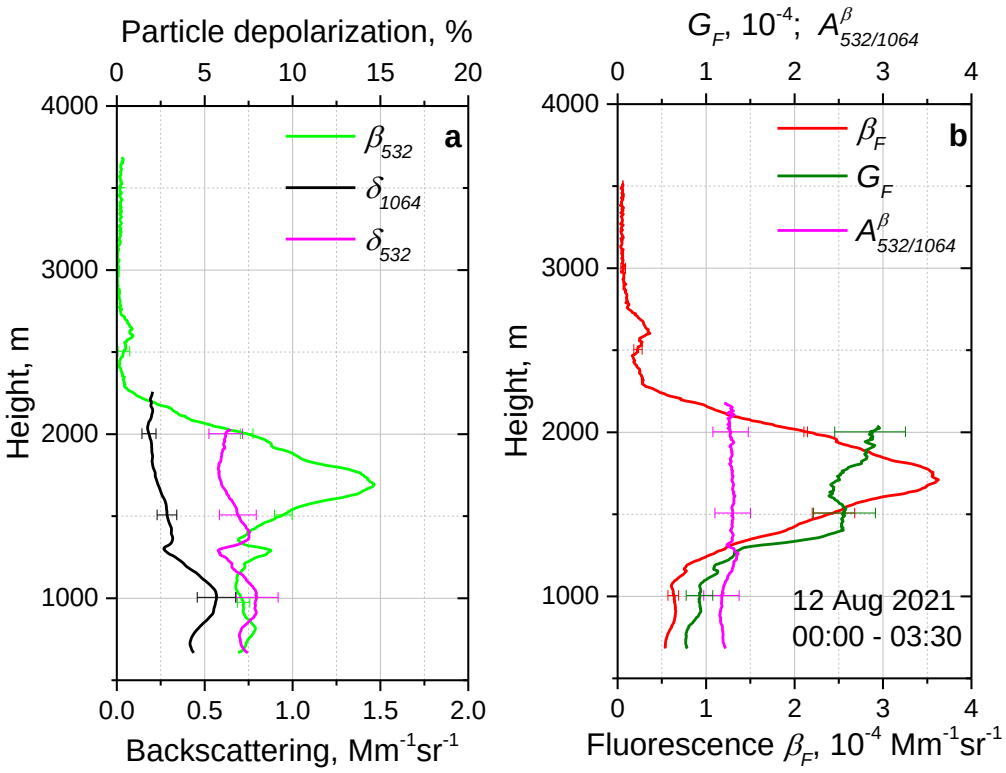

Fig.16. Vertical profiles of (a) backscattering coefficient β_{532} and particle depolarization ratios δ_{532}, δ_{1064}; (b) fluorescence backscattering β_F, fluorescence capacity G_F and backscattering Angstrom exponent $A^{\beta}_{532/1064}$ on 12 August 2021 for period 00:00 – 03:30 UTC.

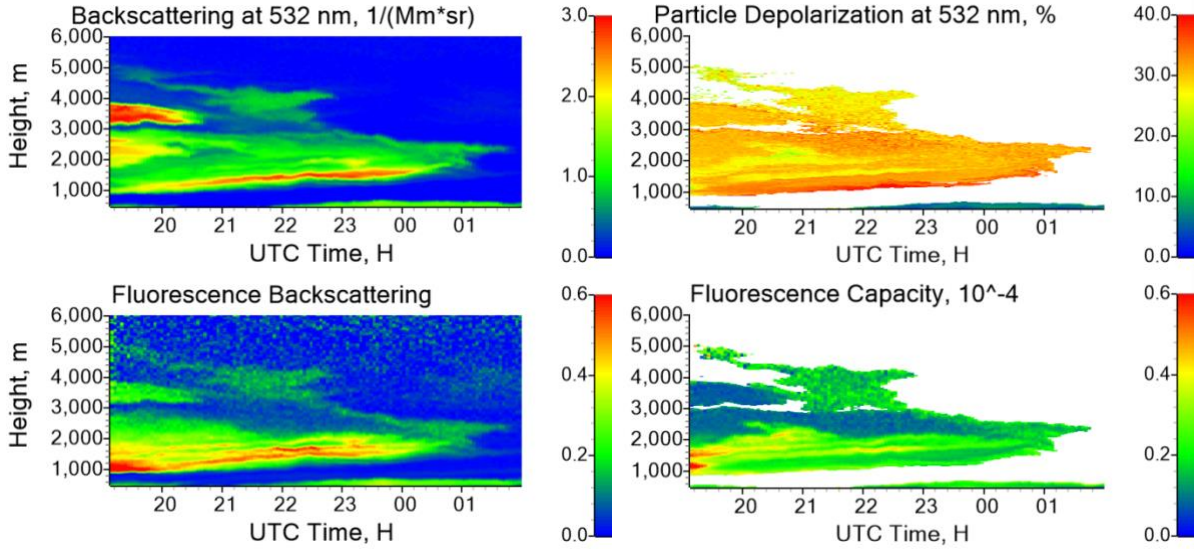

Fig.17. Height – temporal distributions of the backscattering coefficient at 532 nm β_{532}, the fluorescence backscattering coefficient β_F (in 10^{-4} $Mm^{-1}sr^{-1}$), the particle depolarization ratio at 532 nm δ_{532}, and the fluorescence capacity G_F in the night 1-2 April 2021. The values of δ_{532}, and G_F are shown for β_{532}>0.3 $Mm^{-1}sr^{-1}$.

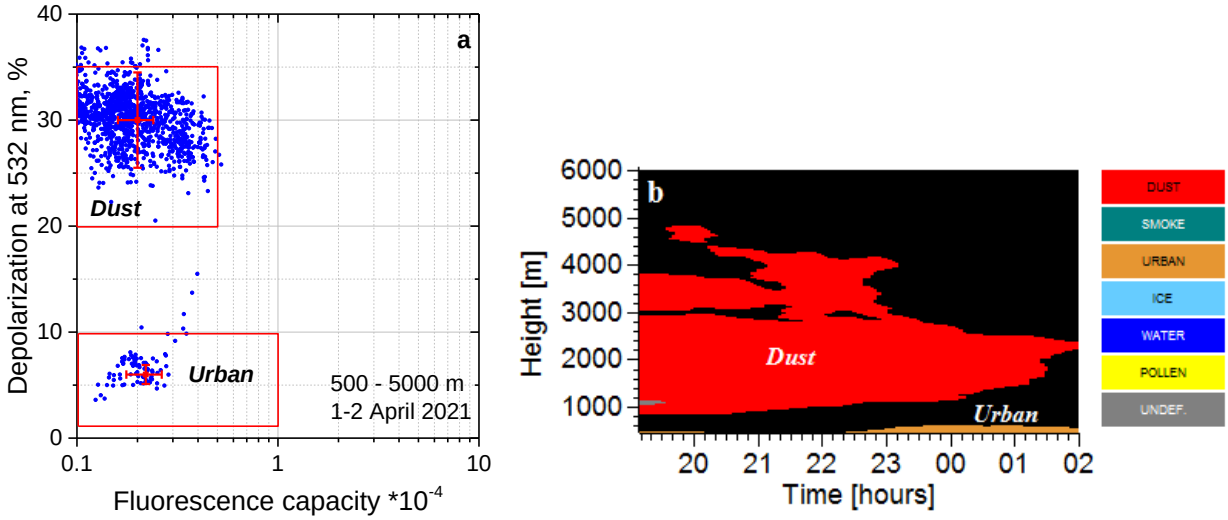

Fig.18. (a) The δ_{532}-G_F diagram for observations in 500 – 5000 m height range and (b) spatio-temporal distribution of aerosol types in the night 1-2 April 2021. Measurements with β_{532}<0.3 $Mm^{-1}sr^{-1}$ are marked by black color.

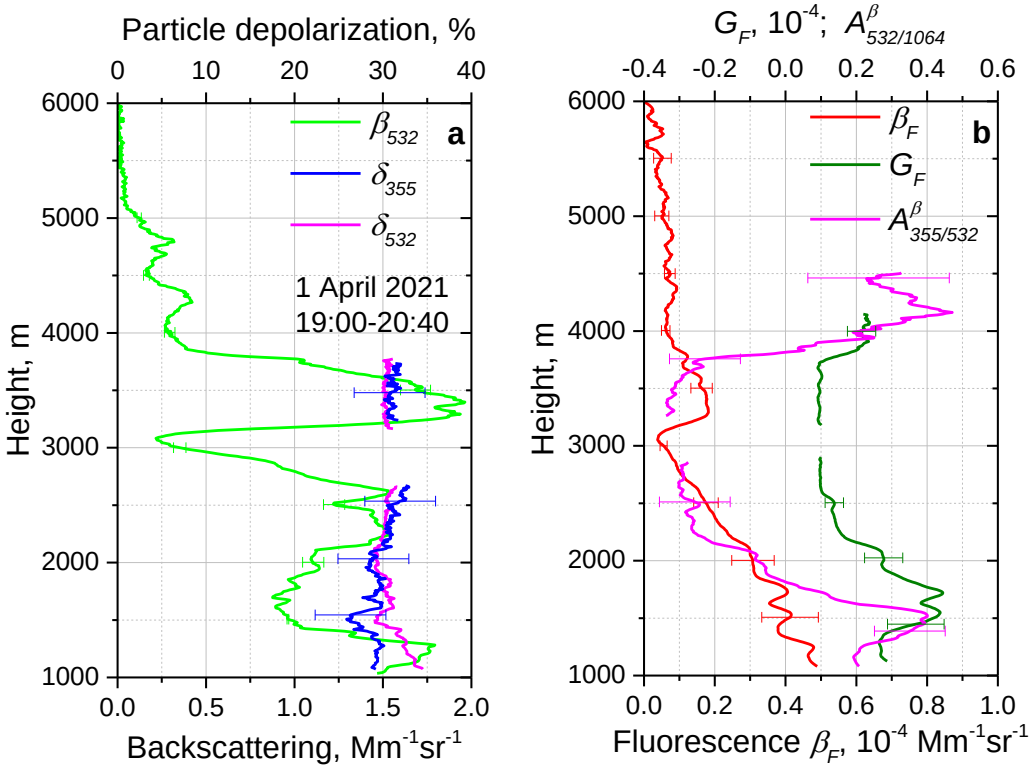

Fig.19. Vertical profiles of (a) backscattering coefficient β_{532} and particle depolarization ratios δ_{532}, δ_{355}; (b) fluorescence backscattering β_F, fluorescence capacity G_F and backscattering Angstrom exponent $A^{\beta}_{355/532}$ on 1 April 2021 for period 19:00 – 20:40 UTC.

Table 1. Ranges of particle depolarization δ_{532} and fluorescence capacity G_F, which were used for aerosol classification.

Aerosol type	δ_{532}, %	G_F, ($\times 10^{-4}$)
Dust	20 - 35	0.1 – 0.5
Pollen	15 - 35	0.8 – 3.0
Urban	1 - 10	0.1 – 1.0
Smoke	2- 10	2.0 – 6.0
Ice	>40	<0.01
Water	<5	<0.01

Table 2. Intensive particle parameters such as the lidar ratios (S_{355}, S_{532}), particle depolarization ratios (δ_{355}, δ_{532}, δ_{1064}), extinction ($A^{\alpha}_{355/532}$) and backscattering ($A^{\beta}_{355/532}$, $A^{\beta}_{532/1064}$) Angstrom exponents for six episodes, analyzed in this work. Parameters are given for chosen height – temporal intervals and the types of aerosol are determined from fluorescence measurements.

Date	Time, UTC	H, km	Type	S_{355}, sr	S_{532}, sr	δ_{355}, %	δ_{532}, %	δ_{1064}, %	$A^{\alpha}_{355/532}$	$A^{\beta}_{355/532}$	$A^{\beta}_{532/1064}$
10.04.2020	21:00-23:00	0.9-1.1 2.0-2.2	Urb.+Poll. Urban	48±7 50±7	48±7 70±10	5.0±1.0 7.0±1.0	6.0±1.0 3.5±0.7	10±1.5 3.0±0.6	1.3±0.2 1.1±0.2	1.4±0.2 2.0±0.2	1.0±0.2 1.2±0.2
30.05.2020	21:00-02:00	1.8-2.0	Urban	60±9	55±8	3.6±0.8	4.0±0.8	5.7±1.0	2.0±0.2	1.6±0.2	1.2±0.2
12.09.2020	20:00-23:00	3.2-3.8	Smoke	50±7	80±12	4.5±1.0	3.0±0.6	2.0±0.4	1.0±0.2	2.2±0.2	1.2±0.2
15.09.2020	00:00-04:00	1.4-1.6 5.8-6.2	Pollen Smoke	40±6 45±7	37±6 70±10	9.5±1.5 9.0±1.5	8.0±1.5 3.5±0.7	15±2.5 1.4±0.3	1.6±0.2 0.8±0.2	1.4±0.2 2.0±0.2	0.9±0.2 1.2±0.2
01.04.2021	19:00-20:40	2.25-2.5	Dust	57±8	52±8	30±4.5	30±4.5	-	0±0.2	-0.3±0.2	-
11.08.2021	22:00-24:00	1.0-1.2 1.5-2.0	Urban Smoke	42±7 45±7	55±8 72±11	- -	8.0±1.2 6.0±0.9	5.7±0.8 2.5±0.5	1.3±0.2 1.0±0.2	1.5±0.2 2.2±0.2	1.1±0.2 1.2±0.2

939
940 Table 3. Intensive particle parameters from publications of Burton et al., (2013); Nicolae et al.,
941 (2018); and Papagiannopoulos et al., (2018) together with values observed in current study for the
942 urban, smoke and dust particles.

	Burton et al., 2013	Nicolae et al., 2018	Papagiannopoulos et al., 2018	This study
	Urban	Continental (rural)	Clear continental	Urban
S_{355}, sr		43-54	50±8	42 - 60
S_{532}, sr	43-81	52-53	41±6	55 -70
$A^{\alpha}_{355/532}$	-	1.2-1.3	1.7±0.6	1.1 -2.0
$A^{\beta}_{355/532}$	-	1.0-1.6	1.3±0.3	1.5 - 2.0
$A^{\beta}_{532/1064}$	0.49-1.3	0.54 – 1.0	1.0±0.3	1.1 - 1.2
Smoke				
S_{355}, sr	-	56-72	81±16	40 - 50
S_{532}, sr	46-87	81-92	78±11	70 - 80
$A^{\alpha}_{355/532}$	-	1.1-1.3	1.3±0.3	0.8 - 1.0
$A^{\beta}_{355/532}$	-	1.4 -2.1	1.2±0.3	2.0 - 2.4
$A^{\beta}_{532/1064}$	0.48-1.6	0.7-0.8	1.3±0.1	1.2
Dust				
S_{355}, sr	-	43-46	58±12	57
S_{532}, sr	41-57	44-49	55±7	52
$A^{\alpha}_{355/532}$	-	0.88-0.92	0.3±0.4	0
$A^{\beta}_{355/532}$	-	0.91-0.97	0.3±0.2	-0.3
$A^{\beta}_{532/1064}$	0.49-0.68	0.16-0.22	0.4±0.1	-

943
944

Appendix. Pollen index provided by SILAM

The SILAM is a chemical transport model, developed by the Finnish Meteorological Institute (Sofiev et al., 2015). It provides information on atmospheric composition, air quality, and pollen. In the pollen module of SILAM, six pollen types (alder, birch, grass, mugwort, olive, ragweed) are considered. The pollen index is defined as a quantitative measure of the severity of the pollen season and a proxy of the allergenic exposure (Sofiev et al., 2012, 2017). This higher the pollen index is, the more pollen grains in the atmosphere and the higher allergy risk. Fig. A1 shows the maps of pollen index in 4 cases. According to the description of SILAM model, the pollen index is labeled as "very high", when its value is greater than 4.0.

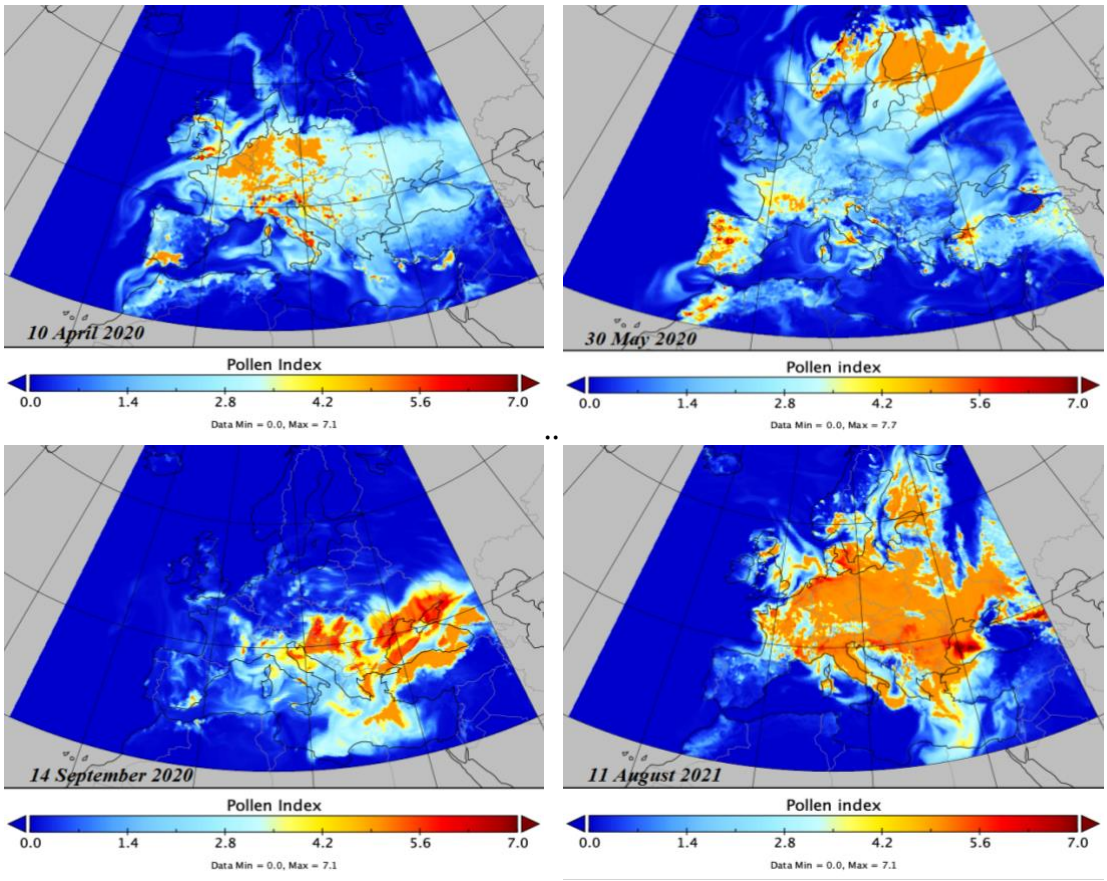

Fig.A1. Pollen index provided by SILAM for 10 April 2020, 30 May 2020, 14 September 2020 and 11 August 2021. The levels of pollen index are – very low (<1.0), low (1.0÷2.0), moderate (2.0÷3.0), high (3.0÷4.0) and very high (>4.0).